

# On time-dependent orbital complexity in gravitational N-body simulations

N. T. Faber<sup>1,2,3\*</sup>, C. M. Boily<sup>1</sup> and S. Portegies Zwart<sup>2,3</sup>

<sup>1</sup>*Observatoire Astronomique, Université de Strasbourg and CNRS UMR 7550, 11 rue de l'Université, 67000 Strasbourg, France*

<sup>2</sup>*Sterrenkundig Instituut 'Anton Pannekoek', University of Amsterdam, Kruislaan 403, 1098 SJ Amsterdam, The Netherlands*

<sup>3</sup>*Section Computational Science, University of Amsterdam, Kruislaan 403, 1098 SJ Amsterdam, The Netherlands*

3 February 2008

## ABSTRACT

We implement an efficient method to quantify time-dependent orbital complexity in gravitational  $N$ -body simulations. The technique, which we name DWaTIM, is based on a discrete wavelet transform of velocity orbital time series. The wavelet power-spectrum is used to measure trends in complexity continuously in time. We apply the method to the test cases  $N = 3$  Pythagorean- and a perturbed  $N = 5$  Caledonian configurations. The method recovers the well-known time-dependent complexity of the dynamics in these small- $N$  problems. We then apply the technique to an equal-mass collisional  $N = 256$  body simulation ran through core-collapse. We find that a majority of stars evolve on relatively complex orbits up to the time when the first hard binary forms, whereas after core-collapse, less complex orbits are found on the whole as a result of expanding mass shells.

## Key words:

$N$ -body simulations – stellar dynamics – chaos

## 1 INTRODUCTION

Computer simulations of the gravitational  $N$ -body problem aim to solve the set of  $3N$  second order ordinary differential equations

$$\mathbf{F}_i = m_i \ddot{\mathbf{r}}_i = -Gm_i \sum_{l=1, l \neq i}^{l=N} \frac{m_l(\mathbf{r}_i - \mathbf{r}_l)}{|\mathbf{r}_i - \mathbf{r}_l|^3}, \quad (i = 1, \dots, N). \quad (1)$$

Here  $G$  is the gravitational constant,  $\mathbf{F}_i$  and  $\ddot{\mathbf{r}}_i$  denote the force and the acceleration exerted by the  $N - 1$  particles  $l$  on particle  $i$  of mass  $m_i$  at position  $\mathbf{r}_i$ . A system with  $N > 2$  is in general chaotic, i.e., the solution to Eq. (1) is known to be sensitive to the initial conditions. Miller (1964) was the first to show that individual orbits calculated from neighbouring initial configurations diverge on a short time-scale proportional to  $4\xi/N$ , where  $\xi$  is the mean time between two subsequent close encounters of a particle. Even when computed with double precision arithmetic, the differences between the two integrations become comparable to the characteristic length- and velocity-scales of the cluster within only a few crossing times. Thus one may argue that the positions and velocities obtained from an  $N$ -body simulation are a fair rendition of the problem at hand in a statistical sense only (Aarseth & Lecar 1975, Quinlan &

Tremaine 1992). Goodman, Heggie & Hut (1993) identify three mechanisms responsible for the exponential growth of the distance between nearby trajectories. Aside from numerical errors<sup>1</sup>, they point out that the exponential instability of the solutions also arises through a fluctuating mean gravitational field, or through inherently chaotic orbits in a static field. However, for systems in dynamical equilibrium and with near-spherical symmetry (such as e.g. globular clusters), they conclude that the principal mechanism responsible for chaos is the cumulative effect of near neighbour interactions, i.e. two-body encounters.

The exponential divergence of the  $N$ -body problem of Eq. (1) has been studied by several authors for systems with up to  $N = 10^5$  particles (Kandrup & Smith 1991; Kandrup & Sideris 2001; Hemsendorf & Merritt 2002). The debate whether Miller's instability is formally caused by chaos is still on-going (see e.g., Kandrup & Sideris 2003; Helmi & Gómez 2007). The assumed chaoticity of such systems may be evaluated by computing the variational equations associated to Eq. (1) (Miller 1971) and by retrieving indicators of chaos such as, for instance, Lyapunov characteristic numbers (Benettin & Galgani & Strelcyn 1976). Other indicators of chaos commonly found in the literature are e.g., the relative Lyapunov indicator (Sándor, Érdi & Efthymiopoulos 2000),

\* E-mail: nfaber@science.uva.nl (NF)

<sup>1</sup> A round-off error at one time step can be considered as a change in the initial conditions for the next time step.

the mean exponential divergence of nearby orbits (Cincotta & Simó 2000) or the small-alignment index (Skokos 2001). All these indicators accurately quantify the exponential divergence of nearby trajectories.

In this work, we propose to investigate time-dependent orbital complexity in an  $N$ -body simulation. We define orbital complexity to be a measure of the richness and non-triviality of the frequency spectrum of an orbit at a given time  $t$ . The possible connection between orbital chaos and orbital complexity has been pointed out by Kandrup, Eckstein & Bradley (1997). In that work, the authors find a strong correlation between their measure of orbital complexity and short time Lyapunov exponents. The notion of complexity provides information about the orbital content of a gravitational system governed by Eq. (1) that is complementary to the classical indicators of chaos mentioned above. For instance, the concept of complexity is exploited by Sideris & Kandrup (2002) to study the continuum limit in the case of large- $N$  simulations. It is used to compare the orbital behavior between particles evolving in smooth potentials and bodies orbiting in the corresponding frozen  $N$ -body configurations. The notion of complexity here allows to contrast the discreteness effects of the  $N$ -body configuration to the orbital evolution obtained in the smooth case. However, whereas a global measure of orbital complexity has been implemented in several works (see e.g., Kandrup et al. 1997), a method to measure the impact of instantaneous changes in orbital complexity has not. A trajectory computed from Eq. (1) can show multiple, qualitatively distinct regimes in time. For instance, an orbit may display arcs of relatively smooth motion such as e.g., an unperturbed parabolic or hyperbolic orbit. At other times, the body may be gravitationally bound in a binary system with a particle of approximately the same mass. Likewise, the body may be temporarily trapped in a complicated higher-order resonance, orbiting about a massive central body. All these states of motion can be identified in time by a suitable measure of complexity. The goal of this paper is precisely to discuss such time-resolved complexity by introducing a dedicated tool for complexity evaluation. The issue of formally relating complexity to chaos will not be addressed here.

Classical spectral methods and Fourier transform based techniques (see Laskar 1993; Carpintero & Aguilar 1998; Valluri & Merritt 1998) are of short execution time and able to provide an accurate frequency domain representation of a given orbit. A global measure of complexity can be retrieved by such an approach. However, the Fourier transform suffers from the problem of losing any time-dependent information on the motion of the particle. In this paper, we present an accurate, easy-to-implement and time-resolved complexity-detection tool for individual orbits in  $N$ -body simulations. A state of dynamical equilibrium is assumed throughout. We implement a specially-adapted method of time series analysis that is based on a discrete wavelet transform. The method post-processes the orbital data of a simulation and provides a time-resolved measure of complexity. The present work mainly focuses on a detailed description of the method and is structured as follows. In Section 2 we introduce the identification technique for time-dependent complexity. Section 3 presents applications to  $N = 2, 3$  and 5-body problems. The analysis of a low-resolution  $N = 256$  equal-mass Plummer

model is presented in Section 4 and a brief discussion of the results is given in Section 5.

## 2 METHOD, TESTS AND VALIDATION

This section presents and tests a technique to quantify time-dependent orbital complexity. In §2.1, we present the discrete wavelet transform (hereafter DWaT) as an efficient tool to determine the base frequencies of an orbit in a time-resolved manner. The indicator of complexity obtained from the DWaT, namely the discrete wavelet transform information measure (DWaTIM), is defined in §2.2.

### 2.1 Wavelet transforms

#### 2.1.1 Definitions

The complexity of motion is analyzed by means of a wavelet transform (see also Gemmeke, Portegies Zwart & Kruip 2008). The use of wavelet transforms has found applications in a wide range of domains such as seismology, financial time series processing or medical electrocardiogram studies; see Hubbard (1998) for further references. A wavelet transform provides a time-frequency representation of a time series  $f(t_q)$  by fitting a wavelet  $\Psi$  to a set of points  $\{t_q\}$ . Whereas Fourier-based methods decompose a signal into infinite sine and cosine functions, effectively losing information at individual times  $t_q$ , the wavelet transform offers precise localization in both the frequency- and time-domain. Wavelet transforms remain band-limited however; they are made up of not one but a limited range of several frequencies.

A wavelet family  $\Psi_{a,\tau}$  is defined by the set of elemental functions generated by scaling and translating a mother wavelet  $\Psi(t)$ :

$$\Psi_{a,\tau}(t) = |a|^{-\frac{1}{2}} \Psi\left(\frac{t-\tau}{a}\right), \quad (2)$$

where  $a$  represents the scale variable and  $\tau$  the translation variable ( $a, \tau \in \mathbb{R}, a \neq 0$ ).

The continuous wavelet transform (CWT) is defined as the correlation between a signal  $S(t) \in L^2(\mathbb{R})$  (the space of square summable functions) and the wavelet family  $\Psi_{a,\tau}(t)$  for each  $a$  and  $\tau$  (see e.g., Daubechies 1992):

$$\langle S(t), \Psi_{a,\tau} \rangle \equiv |a|^{-\frac{1}{2}} \int_{-\infty}^{+\infty} S(t) \bar{\Psi}\left(\frac{t-\tau}{a}\right) dt. \quad (3)$$

Here  $\langle S, \Psi_{a,\tau} \rangle$  denotes the wavelet coefficients and  $\bar{\Psi}$  is the complex conjugate of  $\Psi$ . Equation (3) can be inverted to reconstruct the original time series. The CWT is known to produce a large amount of wavelet coefficients which implies considerable CPU execution times (see e.g., Samar et al. 1999). In addition, the information the CWT displays at closely spaced scales or at closely spaced time points is highly correlated and thus unnecessarily redundant.

For these reasons we instead compute a *discrete* wavelet transform (DWaT). The DWaT offers a highly efficient wavelet representation that can be implemented with a simple recursive filter scheme (Mallat 1999; Daubechies 1992). Unlike the numerical CWT implementation which easily produces more than  $10^5$  coefficients for a single orbital time series of  $Q = 8192$  data points, the DWaT only produces

as many coefficients as there are samples in the time series, i.e.  $Q$ . This property of the DWaT of avoiding redundant wavelet coefficients serves in defining a proper measure of complexity, as we will show in §2.2. For a given choice of the mother wavelet function  $\Psi(t)$  and for the discrete set of parameters  $a_j = 2^j$  and  $\tau_{j,k} = 2^j k$  ( $j, k \in \mathbb{Z}$ ), the wavelet family

$$\Psi_{j,k}(t) = |a_j|^{-\frac{1}{2}} \Psi\left(\frac{t - \tau_{j,k}}{a_j}\right) = 2^{-\frac{j}{2}} \Psi(2^{-j}t - k) \quad (4)$$

defines an orthonormal basis of  $L^2(\mathbb{R})$ . The time series  $f(t_q)$  is sampled at  $Q = 2^J$  ( $J \in \mathbb{N}$ ) constant time intervals of size  $\Delta = t_{q+1} - t_q$ . The discrete wavelet expansion then reads (see e.g., Rosso et al. 2006, Equation [36])

$$f(t) = \sum_{j=1}^J \sum_{k=1}^{2^{j-1}} \langle f(t_q), \Psi_{j,k} \rangle_{\text{discrete}} \Psi_{j,k}(t) \Delta^{-1}. \quad (5)$$

For simplicity we set  $\Delta = 1$  throughout §2. Here  $f(t)$  is the reconstructed signal and  $J = \log_2 Q$  is the number of scales over which the time series  $f(t_q)$  is analyzed. The DWaT coefficients  $\langle f(t_q), \Psi_{j,k} \rangle_{\text{discrete}}$  can be understood as a representation of the wavelet power spectrum (or, energy) at scale  $j$  and time  $t_q$ , associated to the time series  $f(t_q)$ . They represent the local residual errors between successive signal approximations at scales  $j$  and  $j-1$ . In what follows, we set

$$P_j(k) \equiv \langle f, \Psi_{j,k} \rangle_{\text{discrete}} \quad (6)$$

for a more convenient notation of the DWaT coefficients. As mentioned earlier, there are  $Q$  coefficients  $P_j(k)$  and the number of coefficients computed for resolution level  $j$  is  $2^{j-1}$ . The frequency band over which the  $P_j(k)$  are computed is limited by the frequency  $1/(Q\Delta)$  (scale  $j=1$ ) in the low-frequency domain and by the Shannon-Nyquist critical frequency  $f_{\text{cr}} = 1/(2\Delta)$  in the high-frequency domain (scale  $j=J$ ; see also Press et al. 2002, §12.1 and §13.10). We refer to Samar et al. (1999) for further details about the wavelet representation.

We use bi-orthogonal cubic spline functions as mother wavelets (Cohen, Daubechies & Feauveau 1992, case  $\{N, \tilde{N}\} = \{3, 9\}$  in their Table 6.1),

$$\Psi(t) = \sum_l g_l \Theta_3(2t - l), \quad (7)$$

where the  $g_l$ 's are known as basic spline coefficients and

$$\Theta_3(t) = \begin{cases} (t+1)^2/2, & -1 \leq t \leq 0 \\ -(t-1/2)^2 + 3/4, & 0 \leq t \leq 1 \\ (t-2)^2/2, & 1 \leq t \leq 2 \\ 0, & \text{otherwise.} \end{cases} \quad (8)$$

This choice is motivated by three arguments. First and most importantly, spline functions provide an excellent time-frequency localization when compared to other mother wavelet candidates (Ahuja, Lertrattanapanich & Bose 2005; Unser 1999). Instantaneous changes in the dynamics are accurately singled out by the DWaT. We further stress this point in §2.3. Second, the use of splines is computationally inexpensive (Thévenaz, Blue & Unser 2000) and provides further desirable properties such as e.g., compact support and smoothness. (For an exhaustive discussion on spline interpolation, see Unser 1999, Thévenaz, Blue & Unser 2000.) Finally, the use of a bi-orthogonal spline mother wavelet also

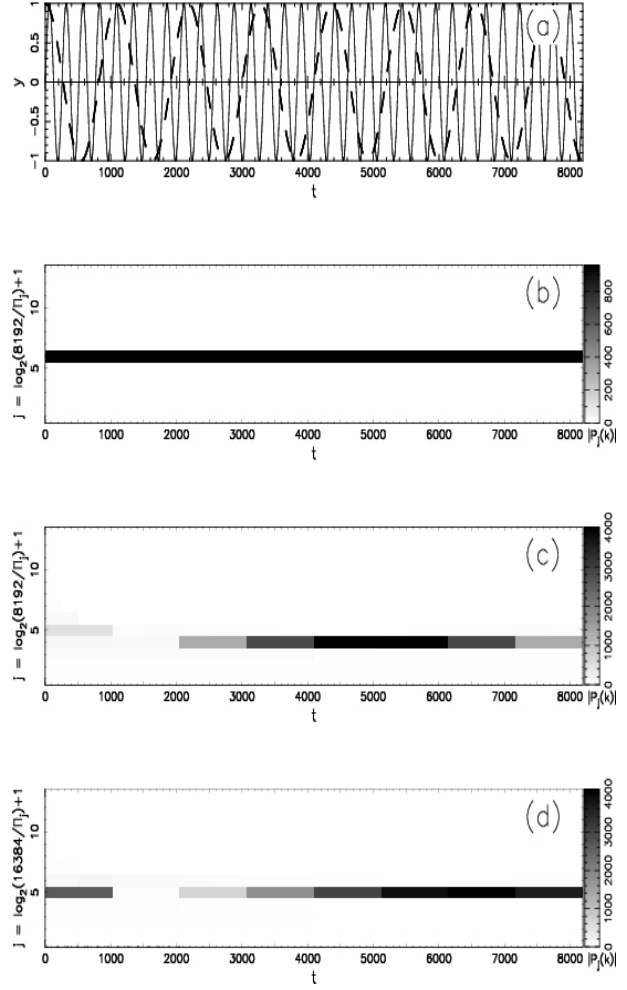


**Figure 1.** Border effects of the discrete wavelet transform (DWaT) of the two sinusoids  $y_1$  and  $y_2$  defined in Eq. 10. From top to bottom: (a) time series of  $y_1$  and  $y_2$  (the dashed line is  $y_2$ ), (b) DWaT of  $y_1$ , (c) DWaT of  $y_2$  with full border effects, (d) DWaT of  $y_2$  with reduced border effects.

implies reduced border effects, an undesired artifact of the wavelet transform algorithm (see §2.1.2 below).

We analyze the velocity time series

$$f(t_q) = v_{\alpha_i}(t_q) \quad (\alpha = x, y, z), \quad (9)$$

i.e. the  $v_{x_i}$ ,  $v_{y_i}$  and  $v_{z_i}$  velocity components of each particle  $i$  ( $i = 1, \dots, N$ ). We do not use the information available on the positions of the bodies since there may be important differences in magnitude between the beginning and the end of these time series. Positional information is then likely to produce pronounced DWaT border effects (see §2.1.2).

### 2.1.2 Border effects

Border effects are an artifact of the wavelet transform algorithm which enforces cyclical boundary conditions on the data vector (Lo Presti & Olmo 1996; Press et al. 2002, §13.10). Such border effects depend on the values held by the two end points of the data vector, and may become important when both ends of the data set differ greatly. In the following, we aim to quantify the extent to which the diag-

nostics become erroneous due to these edge effects.

Figure 1(a) shows the two sinusoids

$$\begin{aligned} y_1 &= \cos\left(2\pi \times \frac{32}{8192}q + \frac{3\pi}{2}\right), \\ y_2 &= \cos\left(2\pi \times \frac{15/2}{8192}q\right), \end{aligned} \quad (10)$$

sampled at  $Q = 8192$  intervals ( $q = 1, \dots, Q$ ). The integration time is commensurate to the periodicity of signal  $y_1$ . This is not the case for signal  $y_2$ . Figure 1(b) and (c) show their respective DWaT scalograms. The scalogram is a grey-shaded representation of the DWaT coefficients  $P_j(k)$ . The darkest shade is for the largest values  $|P_j(k)|$ ; white means  $P_j(k) = 0$ . For both sinusoids a maximum intensity is obtained for the scale that represents the base period  $\Pi_j$  of the respective signal. These are scales  $j = 6$  at period  $\Pi_j = 2^{1-j} \cdot Q\Delta = 2^{-5} \cdot 8192 = 256$  for  $y_1$  and  $j = 4$  for  $y_2$ . The region in which the discrete wavelet transform of  $y_2$  suffers from border effects is known as the cone of influence (Moortel, Munday & Hood 2004). The cone of influence is clearly visible at both edges on Fig. 1(c). On the left-hand edge of Fig. 1(c), for example, the DWaT gives an artificially high excited mode at scale  $j = 5$  up to  $t = 1024$ . The same artifact is also found at scales of higher frequencies, although the magnitude of the effect then diminishes and is barely visible on the left-hand side of Fig. 1(c). In addition, scale  $j = 4$  is wrongly excited in the intervals  $0 \leq t \lesssim 3072$  and  $7168 \lesssim t < 8192$ . The size of the cone of influence depends on the choice of the mother wavelet and is especially significant when the spectrum of the signal contains low frequencies, when the period compares to the overall duration of the time series (Moortel et al. 2004).

Figure 1(d) shows a situation where the border effects have been reduced by extending the integration time to twice the original interval<sup>2</sup>. Doubling the time interval of analysis implies an increased ratio between the signal length and its periodicity. This allows for a higher resolution in the frequency domain (Carmona et al. 1998). Furthermore, a larger portion of the DWaT remains unaffected by the border discontinuity and thus a larger amount of reliable information can be retrieved. In particular, the left-hand and the right-hand border effects are diminished on Fig. 1(d): for instance, the wrongly excited mode at  $j = 5$  between  $0 \leq t \leq 1024$  in Fig. 1(c) has been reduced by  $\approx 82\%$  and the scale  $j = 4$  artifacts of the right-hand side of that figure have vanished completely. In the remainder of this paper, we apply the technique of time series extension whenever the edge effects appear significant. To take into account the remaining artifacts at the beginning of the time series, we furthermore analyze the first  $\approx 2048$  data points (equivalent to the first  $\approx 25\%$  of the signal) of the DWaT analysis with particular caution. Although Fig. 1(d) indicates that border effects may influence more than the first 25% of the  $y_2$  analysis, we found that this is in general not the case for signals produced by  $N$ -body orbits (see §2.2.2 and §3). In what follows, we refer to these 25% of the analysis as potentially biased due to border effects.

<sup>2</sup> Alternately, the  $y_2$  data vector may also be padded with zeros until twice the original time interval is reached.

## 2.2 Measures of complexity

Our goal is to obtain from the DWaT a quantitative estimate of the time-dependent complexity of the frequency spectrum of a trajectory. Exploiting some notions of information theory, we here present the discrete wavelet transform information measure (DWaTIM) as an efficient indicator for complexity. In what follows, we provide a succinct overview of the concept. We follow closely the approach of Rosso et al. (2006) and Martin, Plastino & Rosso (2006). We refer the reader to these works for a more extended discussion.

### 2.2.1 Discrete wavelet transform information measure (DWaTIM)

For a chosen time window of size  $\kappa\Delta$  (where  $\kappa$  is an arbitrary integer) we compute the wavelet energy at each resolution level  $j$ ,

$$E_j = \sum_{k=1}^{2^{j-1}} |P_j(k)|^2, \quad (11)$$

and the total wavelet energy,

$$E = \sum_j E_j, \quad (12)$$

to obtain the so-called relative wavelet energy  $p_j = E_j/E$  at scale  $j$ . The DWaT then provides a probability distribution

$$\mathcal{P} = \{p_j\}, \quad (j = 1, \dots, J), \quad (13)$$

which weighs the base frequency  $j$  in the reconstruction of the original signal  $v_{\alpha_i}(t_q)$ . By definition we have  $\sum_{j=1}^J p_j = 1$ .

The amount of disorder present at time  $t$  in an orbital time series can be quantified by determining the information needed to describe the orbit at that time (Shannon 1948). An information measure (hereafter IM) can be seen as a quantity that describes the characteristics of the time-scale probability distribution  $\mathcal{P}$  of Eq. (13) (Rosso et al. 2006). The IM gives the amount of information required per time unit to specify the state of the system up to a given accuracy. The IM we use in this work is the Shannon entropy (Shannon 1948; Quian Quiroga, Rosso & Basar 1999; Sello 2003)

$$W_S[\mathcal{P}] = -K \sum_j p_j \log_2(p_j), \quad (14)$$

where  $K = 1$  is an arbitrary numerical constant. A minimum of information entropy  $\min(W_S[\mathcal{P}]) = 0$  is obtained if  $p_j = 1$  for some scale  $j$  and 0 for all the remaining scales. This situation only occurs for the ordered dynamics of a periodic orbit with a single base frequency. Likewise, the state of highest complexity is obtained for the case of a white noise signal. For such an orbit, the entire band of base frequencies is sampled by the DWaT in equal proportions, and  $\mathcal{P}$  is characterized by the uniform probability distribution

$$\mathcal{P}_u = \left\{ \frac{1}{J}, \dots, \frac{1}{J} \right\}. \quad (15)$$

In this case the IM is  $\max(W_S[\mathcal{P}]) = W_S[\mathcal{P}_u] = \log_2 J$ . For a given velocity component  $v_{\alpha_i}$  ( $\alpha = x, y, z$ ;  $i = 1, \dots, N$ ) we define the DWaTIM to be the measure

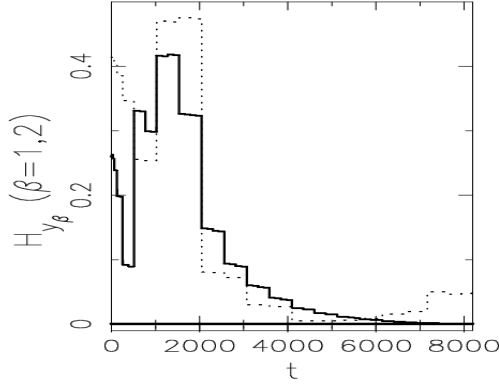


**Figure 2.** Complexity measure for the sinusoids  $y_1$  and  $y_2$  of Fig. 1. The thick solid line confounded with the  $x$ -axis shows the DWaTIM  $H_{y_1}$  as obtained for  $y_1$  from Fig. 1(b). The upper solid line shows the DWaTIM  $H_{y_2}$  obtained for  $y_2$  from Fig. 1(d) in which border effects were reduced by time series extension. The dotted line indicates the  $H_{y_2}$  curve obtained for the case where border effects have not been treated (see Fig. 1[c]).

$$H_{\alpha_i} \equiv \left( \frac{W_S[\mathcal{P}]}{W_S[\mathcal{P}_u]} \right)_{\alpha_i}, \quad (16)$$

i.e. the Shannon entropy for velocity component  $\alpha$  of particle  $i$  normalized to the interval  $[0, 1]$ . The generalized DWaTIM of particle  $i$  is then obtained by taking the arithmetic mean over the 3 components,

$$\Upsilon_i \equiv \frac{H_{x_i} + H_{y_i} + H_{z_i}}{3}. \quad (17)$$

Finally, the overall DWaTIM  $\Upsilon_{\text{tot}}$  of the system is computed by averaging over all particles  $i$ ,

$$\Upsilon_{\text{tot}} \equiv \frac{\sum_{i=1}^N \Upsilon_i}{N}. \quad (18)$$

In what follows we will argue that an increase in DWaTIM correlates with an increase in the complexity of the underlying orbital dynamics at that instant.

### 2.2.2 Complexity of a sinusoid

The temporal evolution of the DWaTIM indicator is computed by subdividing the input signal in non-overlapping time windows of size  $\kappa\Delta$ . We use  $\kappa = 2$ . Figure 2 shows our complexity analysis for the sinusoids  $y_1$  and  $y_2$  of §2.1.2. The DWaTIM of  $y_1$ ,  $H_{y_1}$ <sup>3</sup>, is shown by the lower thick solid line. As expected for a stationary signal with a unique base frequency,  $H_{y_1} \simeq 6.13 \cdot 10^{-4}$ ; the line almost coincides with the  $y = 0$  axis. In what follows, this value can be considered as indicating zero complexity.

We now discuss the pathological case of signal  $y_2$  already mentioned in §2.1.2. The accuracy of the DWaTIM depends on the frequency of the sinusoid. The DWaT has a better resolution at high frequencies (Samar et al. 1999). Conversely, it is more difficult to obtain reliable measures of complexity for signals of low frequencies. In addition, border effects are the most important for such time series (see

§2.1.2). The time series  $y_2(t_q)$  is a long-period, non-cyclical, unique-frequency signal. The DWaTIM  $H_{y_2}$  is shown by the upper solid line on Fig. 2. The line depicts the DWaTIM obtained from the DWaT of Fig. 1(d), i.e. for the case where border effects have been reduced by time series extension. (Note that the border effects for that case still influence the result at all times.) For the first 25% of the diagnostic the effects are dramatic: we find complexity values of up to  $\approx 0.4$ , where  $\approx 0$  is expected. The curve  $H_{y_2}$  approaches zero for  $t \gtrsim 6500$  only. Our method of border effect reduction thus brings little improvement to the quality of the diagnostic for that signal (compared with no corrections at all, cf. dotted line on Fig. 2 obtained from Fig. 1[c]). However, one should bear in mind that the DWaT approach stems from the idea of performing a *multi*-frequency analysis of signals that are well-resolved over the time interval of interest. It is difficult to analyze with the DWaT non-cyclic single-frequency signals of long period such as e.g., signal  $y_{II}$  (see also Moortel, Munday & Hood 2004; Samar et al. 1999). Our analysis of such sinusoids exposed the limits of the DWaTIM method; we here obtained complexity results that were widely biased by border effects. However, in this work we aim to discuss the more generally encountered multi-frequency signals describing orbital motion in the gravitational  $N$ -body problem. For this type of signal, we found that the complexity analysis yields in general consistent results whenever the lowest frequency component of the time series is resolved over at least  $\approx 8$  complete oscillations. Border effects then play a minor role. (For a further discussion of this, see the results obtained for the multi-frequency signals of §2.3, §3.1 or §3.2.)

### 2.3 Toy Models

We illustrate the capability of the method to capture time-dependent changes in the dynamics with two toy models. Let us consider the two time series  $y_I(t_q)$  and  $y_{II}(t_q)$  ( $q = 1, \dots, 8192$ ;  $t_q = q\Delta = q$ ) constructed as follows:

$$y_I(t_q) = \begin{cases} y_A, & 0 < q \leq 4096, \\ y_B, & 4096 < q \leq 8192, \end{cases} \quad (19)$$

and

$$y_{II}(t_q) = \begin{cases} y_A, & 0 < q \leq 1024, \\ y_C, & 1024 < q \leq 3072, \\ y_B, & 3072 < q \leq 4096, \\ y_D, & 4096 < q \leq 6144, \\ y_E, & 6144 < q \leq 8192. \end{cases} \quad (20)$$

The series  $y_I$  and  $y_{II}$  of Eqs. (19) and (20) are made up of 2 and 5 different dynamical regimes, respectively. Each is a different linear combination of Fourier components and white noise:

$$y_A = \sin \left( 2\pi \times \frac{32}{8192} q + \pi \right), \quad (21)$$

$$y_B = \sin \left( 2\pi \times \frac{32}{8192} q + \pi \right) + \sin \left( 2\pi \times \frac{128}{8192} q + \frac{5\pi}{4} \right), \quad (22)$$

$$y_C = \sin \left( 2\pi \times \frac{32}{8192} q \right) + \sin \left( 2\pi \times \frac{128}{8192} q + \frac{\pi}{4} \right)$$

<sup>3</sup> For a more convenient notation, we denote the DWaTIMs obtained for the test cases  $y_\beta$  ( $\beta = 1, 2, I, II$ ) presented in section §2 by  $H_{y_\beta}$ .

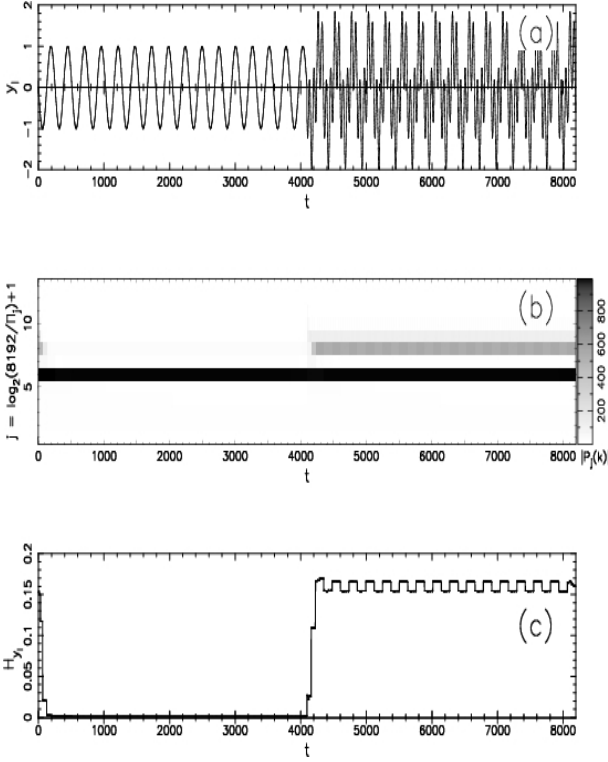


**Figure 3.** Analysis of the time-dependent complexity of the toy model defined by Eq. 19. From top to bottom: (a) time series, (b) discrete wavelet transform, (c) discrete wavelet transform information measure  $H_{y_I}$ .

$$\begin{aligned}
 & + \sin\left(2\pi \times \frac{512/3}{8192}q + \frac{\pi}{8}\right) \\
 & + \sin\left(2\pi \times \frac{8192/17}{8192}q + \frac{\pi}{17}\right), \quad (23)
 \end{aligned}$$

$$y_D = y_C + \mathcal{G}_3(q), \quad (24)$$

$$y_E = \mathcal{G}_1(q). \quad (25)$$

Here  $\mathcal{G}_3(q)$  and  $\mathcal{G}_1(q)$  are Gaussian white noise functions of amplitude unity, zero mean and an absolute variance of 3 and 1, respectively. The complexity increases from one regime to the next: as we go from regime  $y_A$ , through regime  $y_B$  up to  $y_C$ , we double the number of frequency components each time. We then construct  $y_D$  by adding the noise function  $\mathcal{G}_3(q)$  to the  $y_C$  signal. Finally, regime  $y_E$  consists of random numbers only and defines our signal of maximum complexity, i.e. with no underlying periodic signal. In what follows we study the performance of the DWaTIM to capture the time-dependent complexity of the toy models  $y_I$  and  $y_{II}$ .

The complexity analysis for toy model  $y_I$  of Eq. (19) is represented in Fig. 3. Figure 3(a) shows the time series  $y_I(t_q)$ . Until  $t = 4096$ , the signal has the same unique base frequency as the sinusoid  $y_1$  of §2.1.2. However, at  $t = 4096$  the behavior of the signal changes abruptly. A second component, with a frequency 4 times higher than the primary component, is added to the signal. Figures 3(b) and (c) show the associated complexity analysis. The DWaT scalogram of Fig. 3(b) illustrates the power spectrum of the base frequencies  $1/\Pi_j$  as a function of time. The variation of complexity with time of signal  $y_I$  is clearly identifiable, as the increase

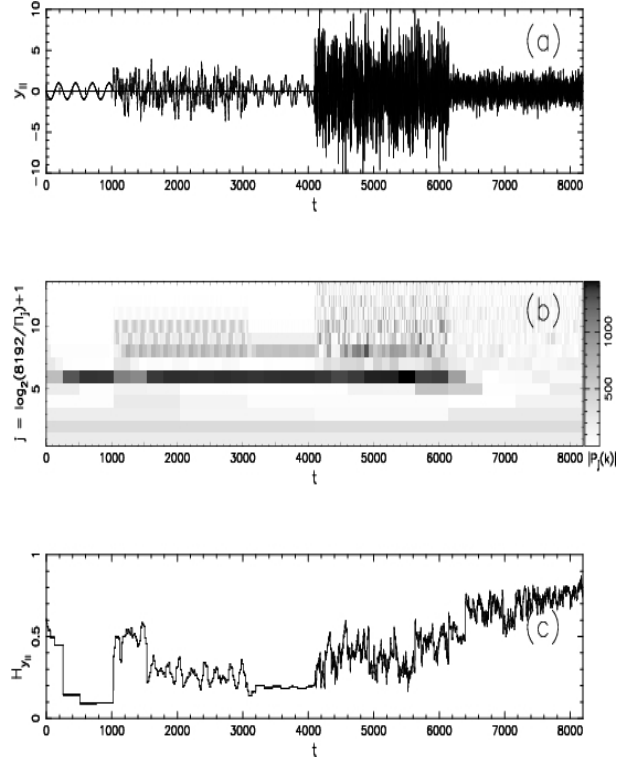


**Figure 4.** Analysis of the time-dependent complexity of the toy model defined by Eq. 20. From top to bottom: (a) time series, (b) discrete wavelet transform, (c) discrete wavelet transform information measure  $H_{y_{II}}$ .

in complexity at  $t = 4096$  is well recovered. The modes represented by scales  $j = 8$  and  $j = 9$  show a response between  $4096 < t \lesssim 8192$ . The related DWaTIM complexity measure  $H_{y_I}$  is plotted in Fig. 3(c). Between  $4096 < t \lesssim 4200$  the complexity rises from  $H_{y_I} \simeq 6 \cdot 10^{-4}$  to an average value of  $H_{y_I} \simeq 0.16$  for  $t > 4200$ . We note that in the time interval  $4096 < t \lesssim 4200$ ,  $H_{y_I}$  rises progressively. The size of this transient interval corresponds to about one half of the period of  $y_A$  which is 256 units. This is the longest of the two periods of the Fourier components involved in the transition  $y_A \rightarrow y_B$ . This sets a limit on the time-localization of the transition. In §3.2 we will discuss in detail the latency of transitions in the dynamics measured by the DWaTIM in an application to small- $N$  problems. We also remark that border effects between  $0 \leq t \lesssim 200$  affect the measure for less than 3% of the signal.

Figure 4 shows the results for the second toy model  $y_{II}$  of Eq. (20). The related time series is shown in Fig. 4(a) and the results for the complexity analysis are represented in Fig. 4(b) and (c). The time-dependent subtleties of the frequency spectrum are depicted by the DWaT in Fig. 4(b). For instance, the drop in complexity at  $t \approx 3072$ , where we remove the two incommensurate base frequencies of regime  $y_C$  and switch to regime  $y_B$ , is recovered. The modes  $j = 10$  and 11, excited between  $1024 \lesssim t \lesssim 3072$  (the  $j = 11$  response during that interval is hardly visible on Fig. 4(b)), do not show a response any more between  $3072 \lesssim t \lesssim 4096$ . The increased complexity between  $y_C$  and its noisy counterpart  $y_D$  is also apparent; scales 7 to 13 show a more irregular pattern between  $4096 \lesssim t \lesssim 6144$  than between

$1024 \lesssim t \lesssim 3072$ . Finally, for the white-noise regime  $y_E$  between  $6144 \lesssim t \lesssim 8192$ , the DWaT response decreases. All the modes  $j = 1, \dots, 13$  are on average less excited than e.g., during regime  $y_D$ , and the DWaT intensity is spread over these scales in an almost uniform manner. This shows that the DWaT correctly identifies this regime as noise. We remark that border effects may explain the feature seen at scale  $j = 6$  between  $0 \lesssim t \lesssim 1536$ , namely, that the magnitude of that mode increases and decreases until it stabilizes at the end of that interval. Therefore border effects may here persist for up to  $1536/8192 \simeq 18\%$  of the duration of the signal. This is still less than the conservative estimate of 25% we have given in §2.2.2. Figure 4(c) shows the DWaTIM  $H_{y_{II}}$ . Apart from the interval  $0 < t \lesssim 1536$  where the border effects spoil the result<sup>4</sup>, the DWaTIM provides a consistent overall diagnostic of time-dependent complexity. Each transition between the regimes  $y_A$  and  $y_E$ , through regimes  $y_C$ ,  $y_B$  and  $y_D$ , is detected by the DWaTIM. For instance, the transition at  $t = 3072$  from  $y_C$  to  $y_B$  corresponds to a drop of about 0.05 in average  $H_{y_{II}}$  magnitude around that instant. We recover a DWaTIM value for regime  $y_B$  of  $H_{y_{II}} \approx 0.19$  between  $3072 \lesssim t \lesssim 4096$  i.e., of about  $3 \cdot 10^{-2}$  units larger than in toy model 1. This 19% difference is due to the response of the three low-frequency scales  $j = 1, 2$  and 3 on Fig. 4 at these times; in toy model 1 these modes do not show any response (see Fig. 3[b] between  $4096 \lesssim t \leq 8192$ ). The performance of the DWaTIM to provide an absolute measure of complexity for a given dynamical regime depends on the time series subjected to analysis and on the number of scales included in the DWaTIM computation. In §3.2 we investigate further this effect for the case of  $N$ -body orbits. Finally, we illustrate the behavior of the DWaTIM in the white-noise limit of  $y_E$ . As mentioned earlier, the total wavelet energy between  $6144 \lesssim t \lesssim 8192$  (see grey-shade intensities on Fig. 4[b]) is reduced with respect to the interval  $4096 \lesssim t \lesssim 6144$ , pointing at the difficulty of the DWaT to single out privileged frequencies with a high probability during  $6144 \lesssim t \lesssim 8192$ . In this limit, the DWaTIM asymptotically reaches its maximum value of 1 (for the case of a perfect white-noise signal and an infinite-length time series; see §2.2.1).

### 3 FEW-BODY ENCOUNTERS

To validate the technique for the case of orbital dynamics, we present three applications to small  $N$  problems ( $N = 2, 3$  and 5). All individual orbits were computed using the **starlab** software environment (Portegies Zwart et al. 2001). Integrations are performed using individual time-steps (Aarseth 1985) and a fourth-order Hermite predictor-corrector scheme (Makino & Aarseth 1992). Time series are constructed by Hermite interpolation at evenly spaced time intervals and by projecting the orbit of each star on the three orthogonal axes  $x$ ,  $y$  and  $z$  in the center of mass coordinate system. Standard  $N$ -body units are used throughout (Heggie & Mathieu 1986).

<sup>4</sup> The measure should give 0 between  $0 < t \lesssim 1024$ . However, it is still true that the signal  $y_A$  is quantified as less complex than  $y_B$  and that the transition from  $y_A$  to  $y_B$  is picked up easily.

#### 3.1 Binary motion: $N=2$

We study independently the motion of two unperturbed, equal-mass binaries with respective eccentricities  $e_1 = 0.05$  and  $e_2 = 0.95$ . Results for the  $v_x$ -component analysis of body #1 of each binary are presented in the left-hand and right-hand panels of Fig. 5, respectively. Figure 5(a) shows the velocity time series  $v_x$  sampled at 8192 regular time intervals. The binaries are integrated over 16  $N$ -body time units, so the sampling interval  $\Delta$  is  $16/8192 = 2^{-9}$ . The period of both binaries is 0.5, allowing a sampling rate of 256 data points per revolution. We note that a consistent choice of  $\Delta$  is of major importance to the method. If an orbit contains frequency components that exceed  $f_{cr}$  (see §2.1.1) the DWaTIM will be aliased. A reasonable selection of  $\Delta$  must thus ensure that the complete dynamics of the system is reproduced for the time-scales of interest.

The complexity diagnostics for the two binaries are given in Fig. 5(b) and (c). The DWaTIM  $H_{x_1}$  is extracted from the DWaT (Fig. 5[b]) and is shown on Fig. 5(c). The complexity measure oscillates in time with the same frequency as the binary (in the same way than for the  $y_I$  toy model of Fig. 3 for  $t \gtrsim 4096$ ). The amplitude of these oscillations is greater for the more eccentric binary. This is so because the larger the eccentricity of a binary the larger the variations in velocity. In the limit where the semi-major axis is sufficiently large, the velocity of both bodies at apocenter is close to zero; likewise, the complexity of any static configuration would asymptotically approach zero. At apocenter we find, for the  $e = 0.05$  binary, a DWaTIM of  $\approx 0$  whereas, for the  $e = 0.95$  case, we obtain a value of  $\approx 0.1$ . In contrast, at pericenter the velocities change rapidly, requiring a broader frequency spectrum and thus implying a higher complexity. Here the DWaTIM indicator increases to  $\approx 0.03$  in the  $e = 0.05$  case and to  $\approx 0.5$  for the  $e = 0.95$  binary. We note that a circular binary ( $e = 0$ ) has a constant velocity modulus: for this case the complexity is zero throughout (for all the regions not affected by border effects, see §2.2.2). We also remark that the time-averaged DWaTIM would give approximately a constant value. This gives a way to quantify an external perturbation acting on a stable Keplerian orbit (see §3.2).

We also computed the average complexity of the  $v_x$ -,  $v_y$ - and  $v_z$ -DWaTIM measures for a total of 100 different binaries. For each binary, the eccentricity and the periodicity was randomly chosen in the intervals  $0 \leq e < 1$  and  $2^{-8} \leq \Pi_j \leq 2$ , respectively. The corresponding results for the DWaTIM are shown by the horizontal lines (in blue) on Fig. 5(c). The solid central line displays the mean DWaTIM; the interval delimited by the upper and the lower dashed line indicates the standard deviation. The average DWaTIM is  $\approx 0.22$ . This value can be seen as indicative for the complexity of unperturbed binaries with a periodicity  $\Pi_j$  comprised within the DWaT bandwidth.

#### 3.2 The Pythagorean problem: $N=3$

The well-studied Pythagorean configuration (Burrau 1913) is a classic example of long-term complex behavior (see e.g., Aarseth et al. 1994). The initial conditions consist of three particles at rest, placed at the vertices of a Pythagorean triangle. The initial conditions are given in Table 1 and the

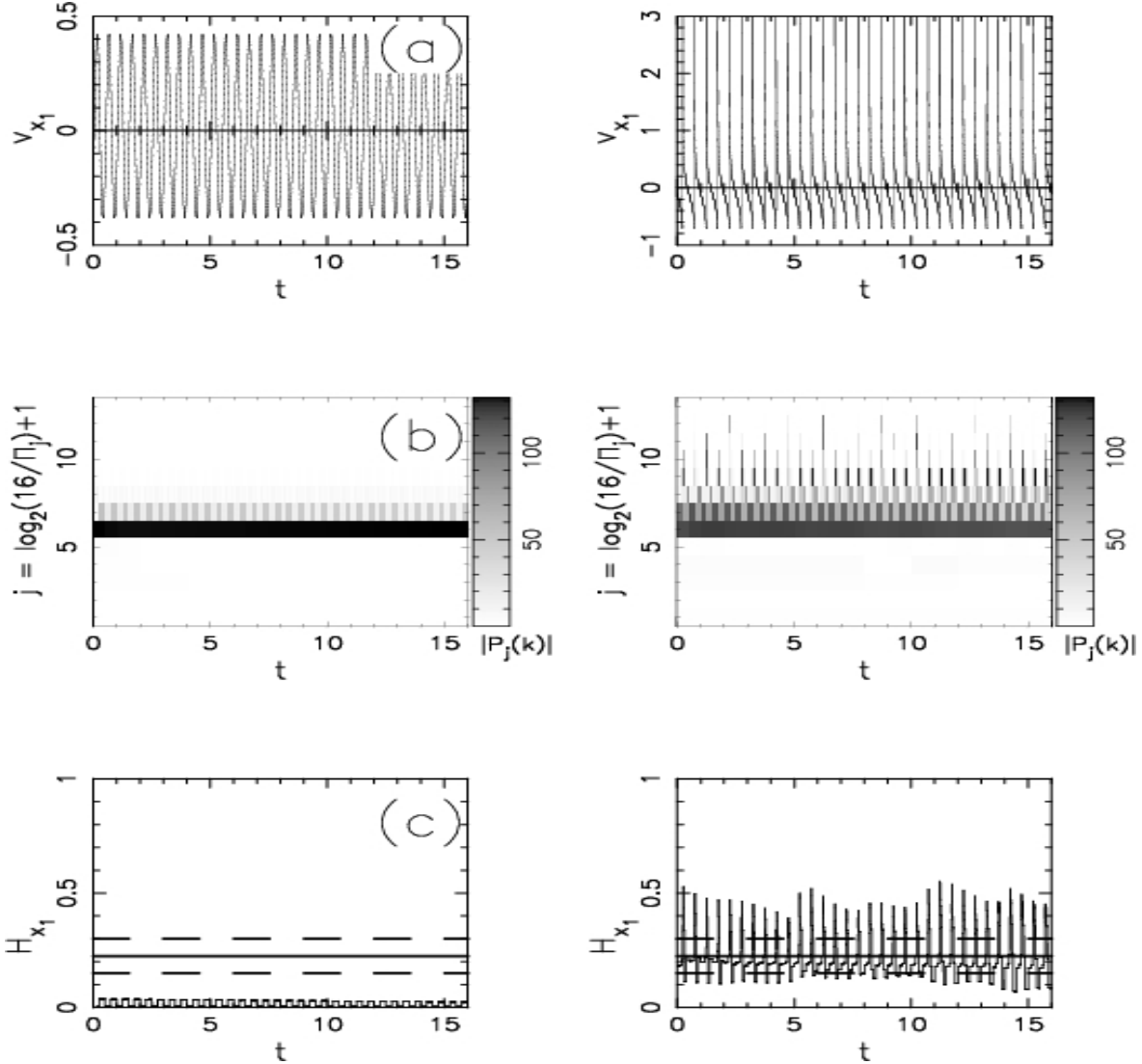


**Figure 5.** Complexity measures of two unperturbed binaries with eccentricity  $e = 0.05$  (left-hand panels) and  $e = 0.95$  (right-hand panels), respectively. For each binary, we show the  $x$ -component result of body #1. From top to bottom: (a) velocity time series, (b) discrete wavelet transform (DWT), (d) discrete wavelet transform information measure (DWTIM)  $H_{x_1}$ . The solid horizontal lines in (c) show the average over the  $x$ -,  $y$ -, and  $z$ -components for 100 binaries with  $e$  and  $\Pi_j$  randomly chosen between  $0 \leq e < 1$  and  $2^{-8} \leq \Pi_j \leq 2$ , respectively. Dashed lines are one standard deviation.

configuration is depicted in Fig. 6.

Orbital integrations were performed over 1500 time units by repeatedly re-running the initial configuration with a reduced per-step integration error until convergence of the result was reached. In this way, the final trajectories showed a total absolute energy error  $|E_{\text{final}} - E_{\text{initial}}|$  of less than  $10^{-10}$ . The analysis is restrained to the first 1024 time units of integration, during which we found by visual inspection that the system spent a comparable amount of time in trivial and in more complicated states. Once more, the time series comprise  $Q = 8192$  data points. Results of the respective time series analysis for particle #1 and for the entire Pythagorean problem are shown in the left-hand and right-hand panels of Fig. 7, respectively.

The  $v_y$ -coordinate of body #1 is shown in the left-hand Fig. 7(a). In the right-hand panel of Fig. 7(a) we illus-

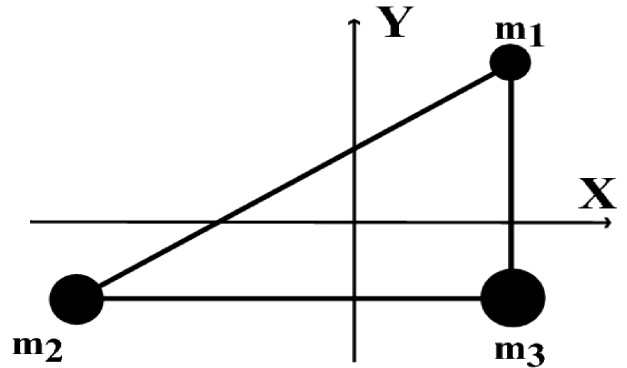


**Figure 6.** Pythagorean problem: initial configuration.



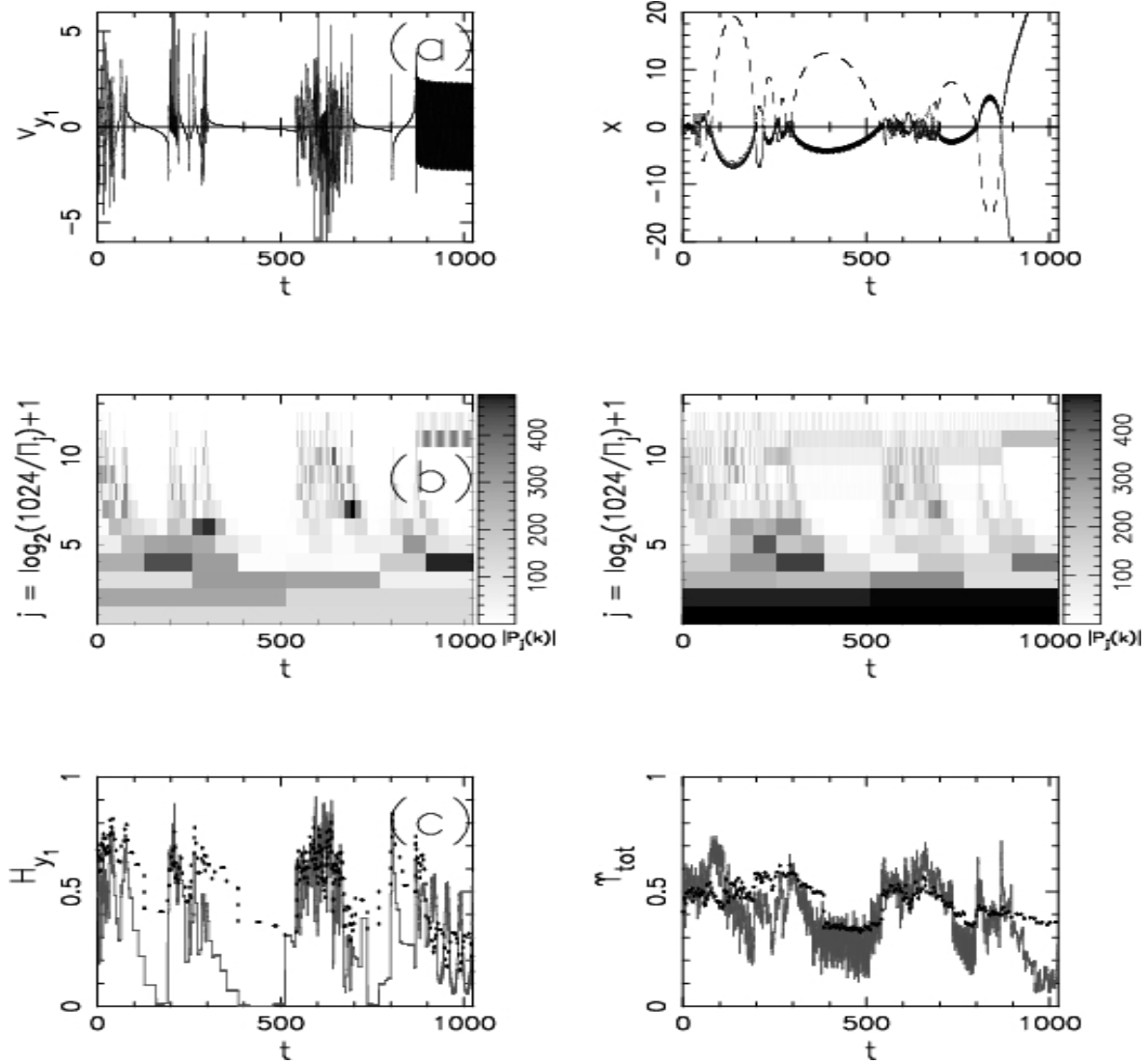


**Figure 7.** Complexity measures of the  $x$  component of particle #1 (left-hand panels) and averaged overall complexity (right-hand panels) of the Pythagorean problem (see Table 1, Fig. 6 and text for further detail). From top to bottom: (a) velocity time series (left-hand panel) and  $x$  position time series of the 3 particles (right-hand panel), (b) discrete wavelet transform (DWT) (left-hand panel) and average DWT (right-hand panel), (c) discrete wavelet transform information measure (DWTIM)  $H_{y_1}$  and average DWTIM  $\Upsilon_{\text{tot}}$ . The dotted lines on (c) are obtained by computing the measures using the complete bandwidth of the DWT. The solid lines show the same result computed by excluding the contribution of scales 1, ..., 4.

Body	mass	$x$	$y$	$z$	$v_x$	$v_y$	$v_z$
#1	3	1	3	0	0	0	0
#2	4	-2	-1	0	0	0	0
#3	5	1	-1	0	0	0	0

**Table 1.** Pythagorean problem: initial conditions.

trate the dynamics of the whole Pythagorean problem by showing the position  $x$  of all the 3 bodies. Here we see that the system is characterized by a highly complicated interplay of the three particles, including a sequence of intermittent binary formation and disruption. In the time interval  $300 \lesssim t \lesssim 540$  for instance, the single body #1 strides away to large distance on a smooth trajectory (upper dashed line in the right-hand Fig. 7[a] during that interval). Due to the

recoil, a binary, formed of bodies #2 and #3, leaves in the opposite direction. The motion of the binary stars about their common centre of mass gives the thick line seen in the lower part of the right-hand Fig. 7(a) between  $300 \lesssim t \lesssim 540$ .

The DWT scalogram of body #1 and the average DWT of the Pythagorean problem (the average magnitude of base frequency  $1/\Pi_j$  at integration time  $t$ ), computed by averaging over the 3 particles and over the  $x$ - and  $y$ -components, are shown in the left-hand and right-hand panels of Fig. 7(b), respectively. The DWTIM for body #1,  $H_{y_1}$ , and the overall DWTIM of the Pythagorean problem,  $\Upsilon_{\text{tot}}$  (see §2.2.1), are shown in Fig. 7(c). The dotted line depicts the DWTIM as computed by taking into account all the scales  $j = 1, \dots, 13$ . The solid line highlights the dramatic improvement of the diagnostic, obtained when ignoring the first 4 scales ( $j = 1, \dots, 4$ ) in the computation. As mentioned

earlier (see §2.2.2), both complexity measures cease to yield reliable results in the limit where the orbit is resolved over less than 8 complete oscillations (i.e., dynamical times). This motivated our decision to exclude the low-frequency DWaT scales in a general manner. We take the conservative choice of not including the  $j = 4$  scale (i.e. the periodicities  $\Pi_4$  corresponding to  $1/8$  of the full signal). For the remainder of this work, we only compute and discuss this improved version of the DWaTIM.

The performance of the DWaTIM can be studied with respect to two criteria: 1) time-localization, i.e. the ability of the measure to identify accurately the instants  $t$  where qualitative changes in the orbital dynamics occur, and 2) continuous quantification of complexity, i.e. the ability of the measure to provide a consistent evaluation of complexity in an uninterrupted manner. In order to discuss 1), we examine the time series of body #1 of the left-hand Fig. 7(a). Let us consider the transitions from a regime where body #1 approaches bodies #2 and #3 on a comparatively smooth trajectory to the more complex regime where it undergoes multiple close encounters with the latter two bodies. By visual inspection of the left-hand and right-hand panels on Fig. 7(a), we identify such transitions to occur at e.g.,  $t \approx 200$ ,  $t \approx 530$  and  $t \approx 800$ . In each of these cases, we can see in Fig. 7(c) that the measure  $H_{y_1}$  shows the corresponding transition. For example, the transition at  $t \approx 530$  is identified by the DWaTIM by an increase of about 0.7. The instantaneous close encounter between the 3 particles at  $t \approx 800$  is also singled out. Here we find a local peak of  $H_{y_1} \approx 0.8$ . Likewise, the instant  $t \approx 875$  at which body #1 forms a binary system with one of the remaining bodies is also recovered; the complexity shows an instantaneous peak at that instant and then gradually decreases from  $H_{y_1} \approx 0.6$  at  $t \approx 875$  to a mean value of  $H_{y_1} \approx 0.25$  at  $t = 1024$ . The accuracy with which the epoch of a transition is resolved depends on the frequency bands involved in the transition. As mentioned earlier, the DWaT resolution in time increases by a factor of 2 when shifting from scale  $j$  to  $j + 1$ . High-frequency transitions can therefore be localized more accurately in time than low-frequency transitions. The maximum latency of the DWaTIM is obtained by studying the particular case of a transition involving the two lower scales  $j = 5$  and 6. The maximum latency then corresponds to the resolution at scale  $j = 6$ , i.e.  $1024/2^5 = 32$  time units. This sets an upper limit to the error on the DWaTIM performance in time-localization. In conclusion, qualitative changes of orbital dynamics can be accurately localized in time by the DWaTIM indicator.

Concerning 2) the continuous quantification of complexity, we argue that, broadly speaking, the  $H_{y_1}$  of the left-hand Fig. 7(c) reproduces the complexity of the frequency spectrum obtained by the DWaT in Fig. 7(b) in a consistent manner. The relative complexity of the time series is quantified continuously in time with respect to the two limiting cases of a single base-frequency sinusoid with  $H_{y_1} = 0$  and a white noise signal of  $H_{y_1} = 1$ . Excluding the low-frequency scales  $j = 1, \dots, 4$  has also some bearings on the reliability of the diagnostics. For instance, when these frequencies are included, the DWaTIM produces inconsistent results in the interval  $300 \lesssim t \lesssim 540$  (see dash-dotted line in Fig. 7[c]). The complexity in the case of unperturbed motion of body #1 is then estimated to be higher than for the case where

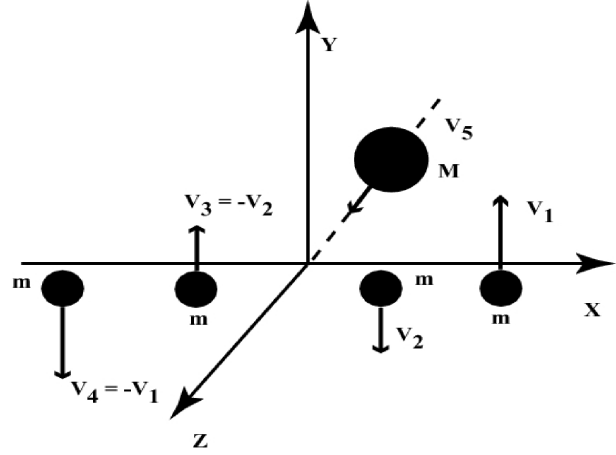


Figure 8. Caledonian 5-body problem: initial configuration.

the body is bound in a binary (compare to the dash-dotted line in the interval  $875 \lesssim t \lesssim 1024$ ).

We also investigated the effects of analyzing the motion of body #1 through a different time series on the  $H_{y_1}$  complexity diagnostic. This additional consistency check allows to measure DWaT border effects for the case of the Pythagorean problem and to examine the extent to which the DWaTIM is able to provide an absolute measure of complexity. To compare two time series we constructed a new one by taking the first half of the  $Q = 8192$  points signal of Fig. 7(a), i.e. up to  $t = 512$ . This gave us a new time series  $v'_{y_1}(t_q)$  of  $Q' = 4096$  data points. The DWaT analysis was then performed over a different frequency domain than for the original  $Q = 8192$  ( $t = 1024$ ) case. The time series  $v'_{y_1}(t_q)$  had also a different end value than its parent time series  $v_{y_1}(t_q)$ , i.e.  $v'_{y_1}(t_{4096}) \neq v_{y_1}(t_{8192})$ . The amplitude of DWaT border effects were therefore different than for the  $Q = 8192$  case (see §2.1.2). We computed the DWaTIM  $H'_{y_1}$  and compared it with  $H_{y_1}$  shown on Fig. 7(c) in the interval  $0 \leq t \leq 512$ . Except for values right at the edge of Fig. 7(c), the results were nearly identical. In particular, the rms residual between the two measures was  $\approx 0.095$  between  $0 \leq t \leq 128$  (corresponding to the first 25% of the signal  $v'_{y_1}$ ) and  $\leq 10^{-3}$  between  $128 < t \leq 512$ .

We obtain similar results for the time series of the other two bodies #2 and #3, and for the  $x$ -component. For that reason we omitted to display those results. The overall DWaTIM  $\Upsilon_{\text{tot}}$  of the Pythagorean problem (shown on Fig. 7[c], right-hand panel) gives a time-resolved insight on the global orbital evolution obtained by integrating the initial conditions of Table 1. Once more, the features seen in the curve of  $\Upsilon_{\text{tot}}$  match those in real space of Fig. 7(a), right-hand side panel. We further discuss the utility of this general measure in the next section §3.3.

### 3.3 Perturbed $N=5$ Caledonian configuration

Next we perturb a configuration of the planar Caledonian symmetric four-body problem (hereafter CP; Széll et al. 2004). Initial conditions are shown in Fig. 8 and in Table 2. The CP is set up as described in Figure 1 of Széll et al. (2004). We specialize to the case where all bodies have masses equal to 1. For this configuration, the unperturbed

Body	mass	$x$	$y$	$z$	$v_x$	$v_y$	$v_z$
#1	1	0.55	0	0.27	0	0.23	0.00
#2	1	0.30	0	0.27	0	-2.42	0.00
#3	1	-0.30	0	0.27	0	2.42	0.00
#4	1	-0.55	0	0.27	0	-0.23	0.00
#5	1.5	0.00	0	-0.72	0	0.00	0.03

**Table 2.** Caledonian 5-body problem: initial conditions.

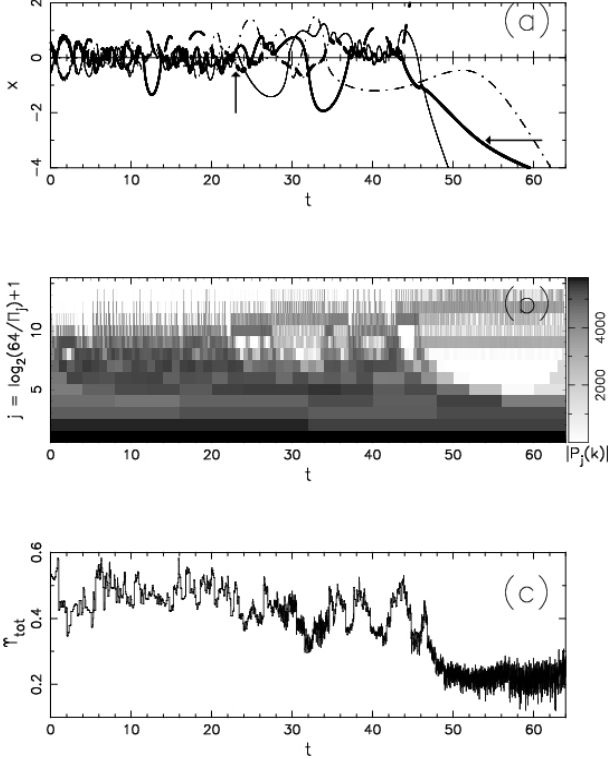


**Figure 9.** Overall complexity of the Caledonian problem (see also Table 2 and Fig. 8). From top to bottom: (a) position time-series of the 5 particles, (b) averaged discrete wavelet transform (DWaT), (c) overall information measure  $\Upsilon_{\text{tot}}$ .

CP consists of two stable binaries evolving in the  $x-y$  plane around their common center of mass. We now perturb the CP configuration with a fifth body of mass = 1.5 (body #5 in Table 2). The perturber approaches the  $x-y$  plane as it moves towards the center of mass of the two binaries on a time scale of  $\approx 8\pi/5$ . At that moment the distance between body #5 and the center of mass is  $\approx 0.15$  i.e., about the separation of the two binaries. Therefore the CP is strongly perturbed from  $t \approx 5$  onwards. The subsequent evolution is characterized by repeated interactions including the formation of hierarchical systems with several particles orbiting around a hard central binary.

The outcome of the complexity analysis is summarized in Fig. 9. Figure 9(a) gives the  $x$ -position time series of the five particles; panels (b) and (c) show the average DWaT and  $\Upsilon_{\text{tot}}$  (similarly to the right-hand Figs. 7[a], [b] and [c]). Figure 9(a) gives an overview of the motion for the entire integration time of 64 time units. (Note that the motion of particle #5, plotted with a dotted line on Fig. 9[a], is difficult to disentangle and is hardly visible.) The intricate gravita-

tional interplay between the five particles is difficult to follow by visual inspection: the individual evolution of the 5 orbits will not be discussed in detail. We focus on the evolution of the system as a whole. The dynamics up to  $t \approx 43$  may be described by roughly two qualitatively different states of motion. The first one is sometimes referred to as “hierarchical interplay” (see e.g., Gemmeke et al. 2006). It is characterized by a central binary and three particles orbiting at large radii. A clear example of this can be seen on Fig. 9 in the time interval  $23 \lesssim t \lesssim 36$ . (The hard central binary forms at  $t \approx 23$  as indicated by the vertical arrow). The second state of motion is what we call “democratic interplay”. This regime is characterized by multiple close encounters between the 5 bodies, each body contributing an approximately equal amount to the overall complexity of the system. Examples of democratic interplay are the time intervals  $5 \lesssim t \lesssim 10$  and  $14 \lesssim t \lesssim 23$ . At  $t \approx 43$ , the dynamics of the perturbed CP changes dramatically. After a close encounter around that time, all the particles stride away to larger distance. One particle immediately escapes the system on a nearly rectilinear trajectory (see upper dashed line on Fig. 9[a] at that instant). The remaining bodies stay close to each other until  $t \approx 46$ , when they are subjected to a further close encounter and another body is ejected (see lower solid line). The subsequent motion is relatively smooth. One particle remains (dashed line) and orbits around a hard binary (indicated by the horizontal arrow).

The overall complexity of the perturbed CP is shown by the DWaTIM in Fig. 9(c). Let us consider two time intervals, prior to and after  $t = 43$ . When  $t \leq 43$  the DWaTIM  $\Upsilon_{\text{tot}}$  is roughly constant and it is interesting to observe that the local minima seen in that time interval can be found during the more quiescent hierarchical regimes, such as for example at  $t \approx 32$ . The two peaks observed at  $t \approx 43$  and  $\approx 46$  arise from the two independent high-energy encounters that we have described earlier taking place at those times. When the final binary forms and the system dissolves the motion becomes unmistakably less complex and consequently  $\Upsilon_{\text{tot}}$  has a lower value of  $\approx 0.2$  on average for all time  $t \gtrsim 48$ .

#### 4 EQUAL MASS $N=256$ PLUMMER SPHERE

We apply the DWaTIM technique to a self-gravitating spherical polytrope of index  $n = 5$  (Plummer 1911; Binney & Tremaine 1987, §4.4.3). The phase-space distribution function  $\mathcal{F}$  of this system is a power-law of  $\varepsilon$ ,

$$\mathcal{F}(\varepsilon) = \frac{24\sqrt{2}}{7\pi^3} \frac{R^2}{G^5 M^4} (-\varepsilon)^{\frac{7}{2}} \quad (26)$$

where  $\varepsilon = \frac{1}{2}v^2 + \Phi(r) < 0$  is the mechanical energy per unit mass,  $v$  the three-dimensional velocity,  $\Phi$  the potential which is a function of the radius  $r$  only. Note that  $\mathcal{F} = 0$  by construction whenever  $\varepsilon > 0$  so that only mass elements bound by gravity are considered. Given a value of the gravitational constant  $G$ , the two free parameters  $M$  and  $R$  define the total system mass and a reference unit of length, respectively. Integrating  $\mathcal{F}$  over all velocities at constant radius yields the mass density  $\varrho$  at that radius,

$$\varrho(r) = \int_0^{\sqrt{-2\Phi(r)}} 4\pi \mathcal{F}(\varepsilon) v^2 dv = \frac{3}{4\pi} \frac{M}{R^3} \left(1 + \left[\frac{r}{R}\right]^2\right)^{-5/2} \quad (27)$$

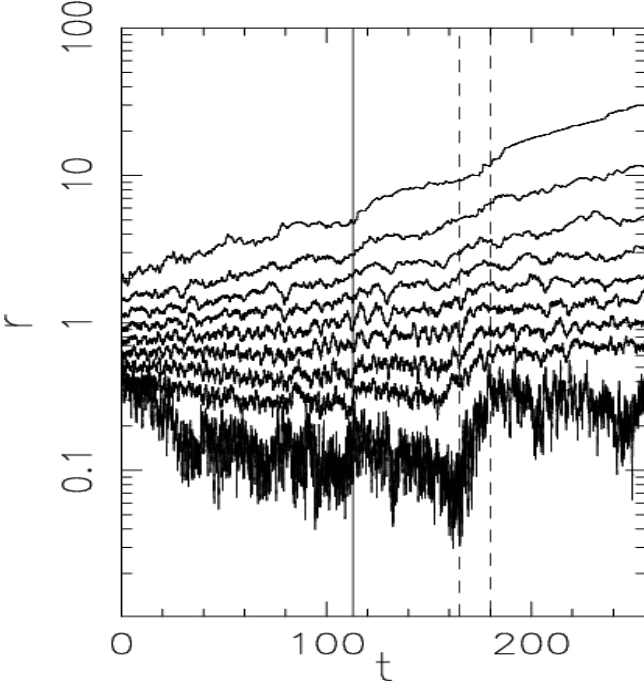


**Figure 10.** From bottom to top: core radius  $r_c$ , 20%, 30%, 40%, 50%, 60%, 70%, 80% and 90% Lagrangian radii of the  $N = 256$  equal-mass Plummer sphere. The solid vertical line at  $t = 113$  marks the formation of the first hard binary in the system. The dashed vertical lines indicate the onset and the end of a notable core expansion between  $165 \lesssim t \lesssim 180$ .

where we have used  $d^3v = 4\pi v^2 dv$  valid for an isotropic velocity field and where we have substituted for  $\Phi(r)$  by solving Poisson's equation. Note that the length  $R$  defines the radius of a uniform-density core ( $\rho[r \ll R] \approx \text{constant}$ ). An  $N = 256$  particle representation of Eq. (27) is obtained by random-sampling the mass density to assign three-dimensional positions. All bodies have mass  $m_i = M/N$ , where  $i = 1, \dots, N$ . The particles' energy is attributed similarly from Eq. (26) from which we compute the square velocity  $v^2 = 2(\epsilon - \Phi[r])$  as in the standard method of Aarseth, Hénon & Wielen (1974). In those circumstances the total kinetic and gravitational energies satisfy the virial theorem of equilibrium systems.

The nominal dynamical time is  $t_d = 2R/\sigma$  where  $\sigma^2$  is the mean squared velocity averaged over mass up to the half-mass radius. We found  $\sigma^2 = 0.392...GM/R \simeq \pi GM/8R$ . The two-body relaxation time is conveniently defined as  $t_r = Nt_d/\ln 0.4N$  (see Binney & Tremaine 1987). If we set Heggie-Mathieu computational units with  $G = M = 1$  and  $R = 1.1781$  such that the total binding energy  $E = -1/4$ , we obtain  $t_d \approx 3.46$  so that for  $N = 256$  bodies the relaxation time  $t_r \approx 191$  time units. For low- $N$  systems such as this one, the diffusion of kinetic energy leads to core-collapse on roughly that time scale, when  $\rho$  becomes singular at the center. It is around that time that hard binaries form and energy exchanges between bodies is at its most extreme. We therefore evolved the system for a total time of 256 time units to ensure that the cluster reaches core-collapse and contrast pre- and post-collapse evolution. The equations of motion were integrated with no softening of the potential.

The velocities of all bodies are stored at regular time intervals and the DWaTIM is computed in a post-simulation analysis. The sampling interval,  $\Delta$ , should be sufficiently small to capture the dynamics in the dense core fully. A naive strategy would be to store all data at all integration time steps. For the configuration adopted here we have observed that the time steps may become as small as  $2^{-32} \simeq 2.32 \cdot 10^{-10}$ ; unfortunately a sampling rate of that order would translate to a prohibitively high volume of data storage even for modest values of  $N$ . Instead, we note that the dynamical time  $t_d$  in principle sets a standard from which to pick an adequate value of  $\Delta$ . But because the central region becomes ever denser during evolution,  $t_d \approx 3.46$  set from the initial configuration would give no useful reference.

Instead, we explore the evolution in time of the mass profile of the system and look for a minimum core length and velocity dispersion inside that core. The density-averaged core radius  $r_c$  defines a quantity which monitors the rise of the central density (see e.g. von Hoerner 1960, Casertano & Hut 1985). From Eq. (27) we find for the initial configuration  $r_c = R/2 \simeq 0.59$  (enclosing 13% of the mass, or 33 bodies). Figure 10 displays the time-evolution of  $r_c$  and several Lagrange radii. The core radius  $r_c$  always appears at the bottom on Fig. 10. Up to  $t \approx 113$  units,  $r_c$  decreases on the mean. At that time, the first hard binary of binding energy  $E < -100kT$  forms<sup>5</sup>. That event is marked with a vertical full line on Fig. 10. Note that  $r_c$  along with the 20% and 30% Lagrange radii increase significantly from  $t \approx 165$  onwards. This phase of rapid expansion indicates the on-set of post-collapse evolution for that simulation. The minimum value of  $r_c \simeq 0.05$  occurs at  $t \simeq 165$  units and encloses 3% of the total mass (8 bodies). We compute a dynamical time  $t_{d,c} \simeq 0.05$  for the core at that time, a factor  $\simeq 70$  smaller than the value computed from the initial conditions. An orbit confined to the core is adequately sampled with five points or more and hence we set  $\Delta = 0.01$  for the complexity analysis. The time-resolution of any features seen in the diagnostic of complexity is therefore  $2\Delta = 0.02$  units, and any binary formed through dynamical evolution is well sampled provided its binding energy  $E > -2.75kT$ .

#### 4.1 Individual orbits

To illustrate the differences in orbital complexity a star may show between the initial time and the moment of core expansion, we graph in Fig. 11 the  $x-y$  projections of 2 individual orbits during two windows of four time units, the first running from  $t = 0$  to 4 (top panels), the second running in the interval  $t = 160$  to 164 (bottom panels). We picked two stars that happened to orbit within the core in each time interval (the circles on the figure indicate  $r_c$  at the times shown). In both the cases displayed the orbit starts off smooth and regular, but traces a much more intricate pattern later on.

These trends can be identified in a graph of the DWaTIM for these and four other orbits as displayed on Fig. 12. The figure shows  $v_x$  vs time in the main frames and the DWaTIM as the top inset frame for each case. Note the

<sup>5</sup> The energy scale  $kT$  is defined by the condition that the total stellar kinetic energy of the system, excluding internal binary motion, is  $3/2NkT$ .

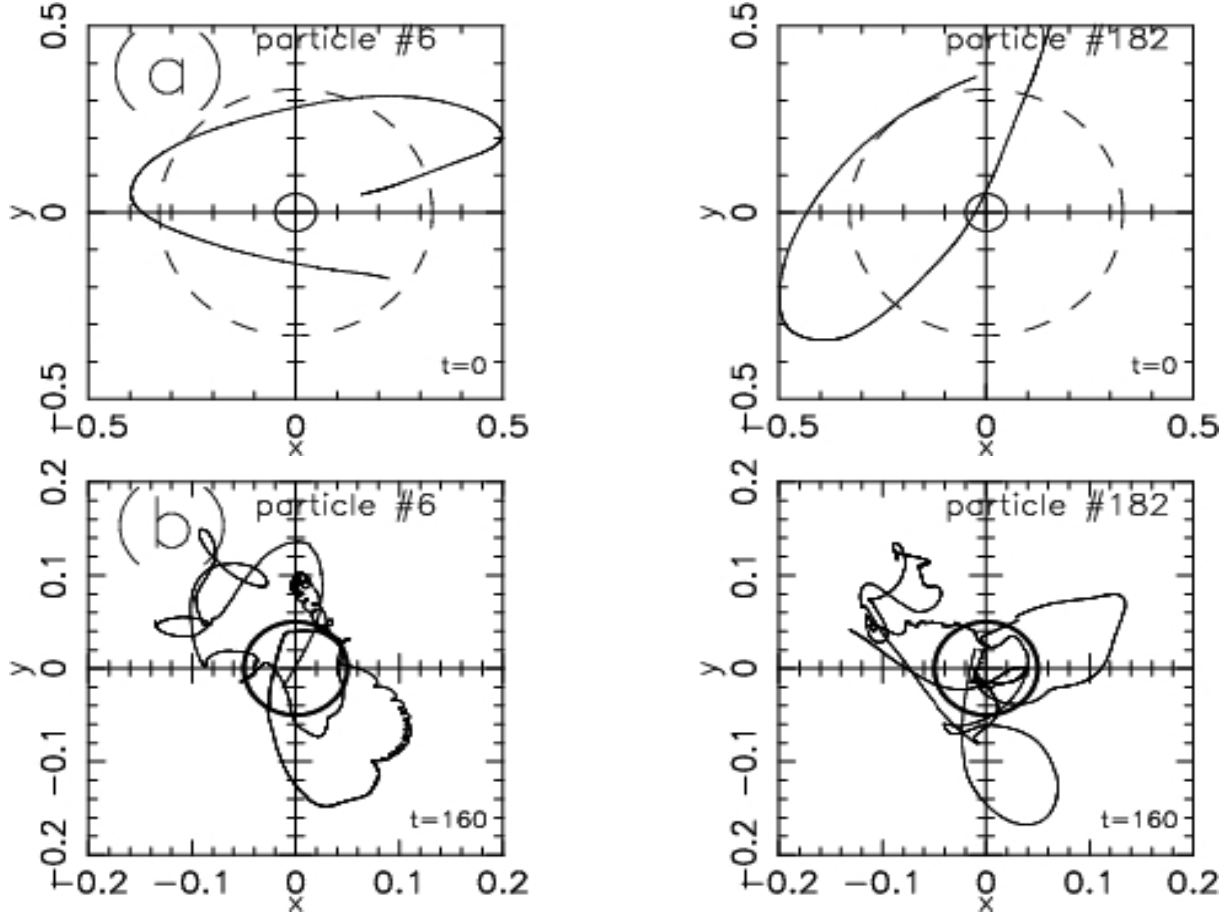


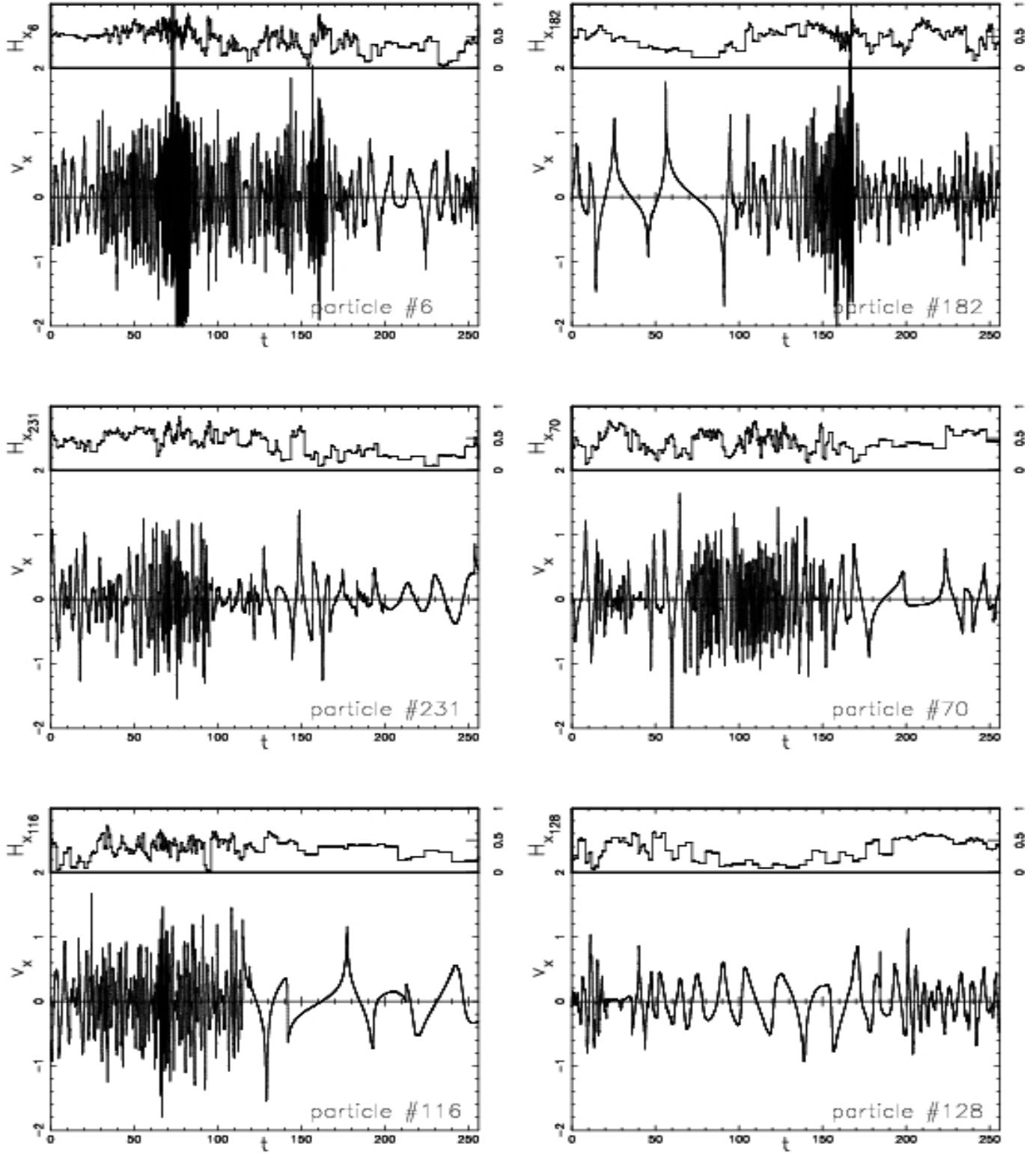
**Figure 11.** Two stars evolving in the core of the  $N = 256$  equal-mass Plummer sphere: (a) the  $x - y$  projections of particles #6 and #182, evolving in the core over 4 time units starting at  $t = 0$ , (b) their  $x - y$  projections starting at  $t = 160$ . The outer dashed circle in (a) shows the core radius  $r_c$  of the cluster at  $t = 0$ . The inner circle in (a) depicts the core radius at  $t = 160$  as shown in (b) and illustrates the difference in scale between the two figures.

change of scales: the DWaTIM is plotted against the scale shown at the right-hand side of each figure. Focusing on the top two panels on Fig. 12, we can identify the more complex phases around  $160 \lesssim t \lesssim 164$  of the orbits displayed on Fig. 11(b) as local peaks in the DWaTIM during this time interval. It is clear that stars set on regular orbits initially can show more complex behavior at later times. The opposite is also possible, as we illustrate in Fig. 12 with four more orbits also orbiting in and out of the core region. These and many others not shown here are typical of the wide variety of DWaTIM spectra: some orbits show rapid fluctuations in  $v_x$  and yield a rather broad band of base frequencies (especially particles #6 and #182). Other trajectories have a narrower spectrum of frequencies (e.g., particle #128).

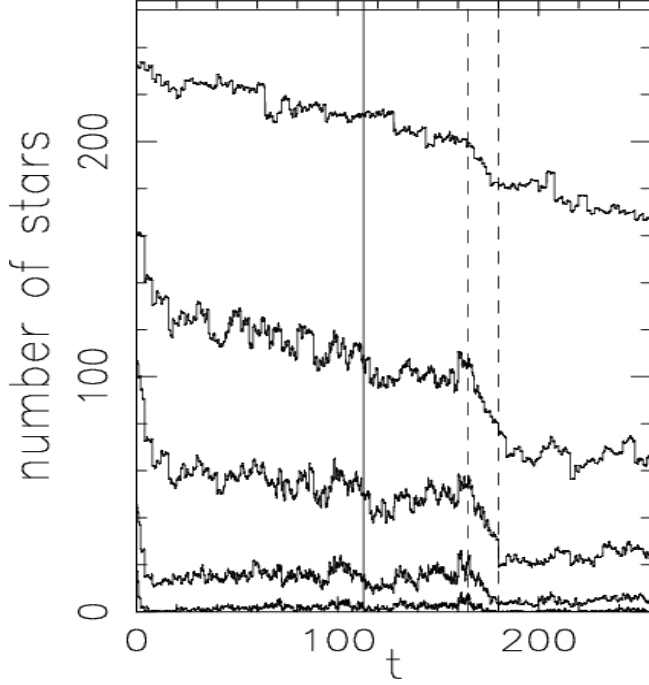
#### 4.2 Global behavior of the Plummer sphere

Fig. 13 shows as a function of time the cumulative number of stars whose DWaTIM  $\Upsilon_i$  ( $i = 1, \dots, N$ ) exceeds a given threshold. The uppermost horizontal line on the figure denotes the total number of stars. The broken curves are for (from top to bottom)  $\Upsilon_i > 0.2$ ,  $0.4$ ,  $0.5$ ,  $0.6$  and  $0.7$ . Once more, the vertical solid and dashed lines indicate the time when a hard binary first formed and the interval of

post-collapse core expansion, respectively (cf. also Fig. 10). Broadly speaking, the orbital complexity decreases on the mean with time. The uppermost lines showing  $\Upsilon_i > 0.2$  and  $\Upsilon_i > 0.4$  decrease monotonically save for small localised fluctuations. In all the cases displayed, a pronounced drop in complexity is seen throughout the phase of core expansion, at times  $160 \lesssim t \lesssim 185$ . For instance, at the beginning of the expansion, about 110 stars have  $\Upsilon_i > 0.4$  whereas at  $t \approx 180$  only 75 stars reach that level. The situation is similar for higher-threshold curves. After the formation of a hard binary but prior to post-collapse expansion, i.e. in the interval  $113 \lesssim t \lesssim 165$ , the complexity levels off or increases slightly with time. For example, the number of stars with  $\Upsilon_i > 0.5$  increases from about 40 to approximately 55 stars in that interval. Hence, orbits that are already relatively complex at the time of binary formation yield a DWaTIM of even larger amplitude up to core-collapse and the on-set of the expansion phase. This trend is also found in the curve  $\Upsilon_i > 0.6$  and to a lesser extent in the  $\Upsilon_i > 0.7$  curve. It may be important to note that the global results of Fig. 13 are not in contradiction with the apparent trend of increasing complexity depicted by the two stars of Fig. 11. Stars #6 and #182 of that figure are both part of the 8 stars that happen to reside in the core around  $t \approx 165$ . At these times the stars



**Figure 12.** Time evolution of 6 individual orbits in an  $N = 256$  equal-mass Plummer sphere model. Each figure shows the complexity diagnostic obtained with respect to the  $x$ -coordinate of particle  $i$ , and comprises the velocity time series  $v_{x_i}$  (solid line in red, plotted against the left-hand axis) and the DWaTIM  $H_{x_i}$  (solid blue line in the upper inset, plotted against the 0 – 1 scale shown on the right-hand axis).



**Figure 13.** Cumulative number of stars of the  $N = 256$  equal-mass Plummer sphere with a DWaTIM  $\Upsilon_i$  ( $i = 1, \dots, N$ ) larger than (from top to bottom) 0.2, 0.4, 0.5, 0.6 and 0.7, respectively. The uppermost horizontal line shows the total number of particles  $N = 256$ . The solid vertical line at  $t = 113$  marks the formation of the first hard binary in the system. The dashed vertical lines indicate the phase of core expansion ( $165 \lesssim t \lesssim 180$ ).

have a high DWaTIM with values of  $\Upsilon_6$  and  $\Upsilon_{182} > 0.6$  (see also the two upper panels of Fig. 12). Stars #6 and #182 therefore contribute to the local peak of the  $\Upsilon_i > 0.6$  curve observed on Fig. 13 around  $t \approx 160$ . The snapshots given in Fig. 11(b) do not reflect a progressive increase in orbital complexity of the Plummer sphere between  $0 < t \leq 164$ . The enhanced two-body scatter attributable to the newly formed binary can be directly measured by the DWaT. In conclusion, both that event and the on-set of post-collapse expansion can be singled out on Fig. 13 as a local minimum and a local maximum, respectively, in runs of the cumulative  $\Upsilon_i$  (as exemplified, for instance, by the curve of  $\Upsilon_i > 0.5$ ).

A scalogram of the DWaT averaged over all  $N = 256$  Plummer sphere particles is shown on Fig. 14. The dark shade illustrates base frequencies  $1/\Pi_j$  of high amplitude, white means zero amplitude (see also §3.2 and §3.3). Figure 14(a) brushes a global picture for all scales  $j = 1, \dots, 15$ , whereas Fig. 14(b) depicts only the high-frequency scales  $j = 11, 12$ , and 13. Some modes are growing in intensity and are then fading away after  $t \simeq 165$  units when the core starts to expand. A particularly good example is the scale  $j = 6$  which reaches progressively higher amplitude in the interval  $0 \lesssim t \lesssim 160$  before fading away during the expansion phase of the inner volume of the sphere. The onset of expansion triggers high-frequency modes (cf. Fig. 14[b]) which reflect the evolution toward more anisotropic radial orbits. Radial anisotropy implies more eccentric motion relative to the centre of mass and an enhanced spectrum of frequencies, cf. Fig. 5.

An illustration of the global measure of complexity

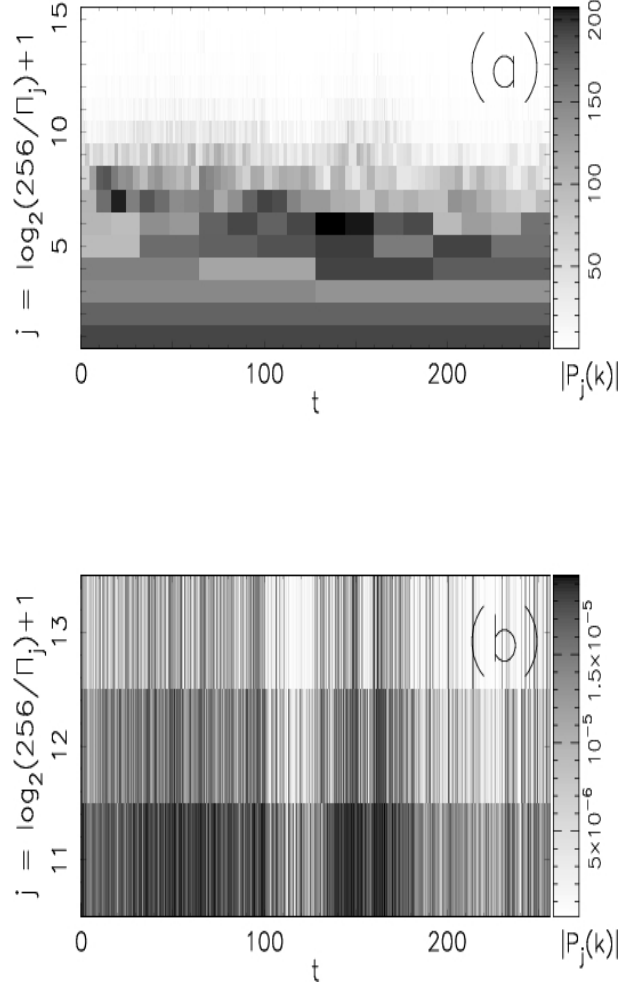


**Figure 14.** Average discrete wavelet transform (DWaT) of the  $N = 256$  Plummer sphere as a function of time. The averaging is performed for a total of 768 time series, i.e. over all particles and over the three velocity components. The figure illustrates the average amplitude of base frequency  $1/\Pi_j$ : (a) the complete DWaT scalogram (scales  $j = 1, \dots, 15$ ); (b) zoom on the high-frequency scales  $j = 11, 12$ , and 13.

$\Upsilon_{\text{tot}} = \sum_i \Upsilon_i / N$  is shown on Fig. 15. The solid and dashed vertical lines denote the same transitional phenomena as in all preceding figures. On the whole, the curve of the DWaTIM depicts the same global decrease in complexity as observed on Fig. 13. A close inspection of Fig. 15 suggests three different regimes in the evolution of the DWaTIM indicator  $\Upsilon_{\text{tot}}$ :

- Regime 1 takes place between  $0 < t \lesssim 165$ . In the interval  $0 \leq t \lesssim 20$ , we observe a rapid drop in  $\Upsilon_{\text{tot}}$  which has no clear origin in a physical phenomenon (binary formation, core-collapse, etc). The equilibrium cluster has a dynamical time  $t_d \simeq 3.5$  and hence the elapsed time  $t = 20$  is  $\approx 8t_d$  or eight orbital times, a further illustration of border effects arising from a too-short time of integration. For  $t \gtrsim 20$ , the curve decreases on average until  $t \simeq 110$  when a slower but constant decline sets in. The DWaTIM  $\Upsilon_{\text{tot}}$  decreases from  $\approx 0.38$  at  $t \simeq 20$  to  $\Upsilon_{\text{tot}} \approx 0.35$  at  $t \simeq 165$ ; the formation of soft- and hard-binaries therefore has little impact on the *global* complexity of the system. That being

said, it is difficult to disentangle the apparent trend of a drop in complexity during regime 1 because, first of all, the rapid drop early on is attributable to border effects; and second, the time scale over which the trend becomes significant is comparable to the two-body relaxation time for that system. The data on Fig. 15 may be best understood in the light of Fig. 13. In that figure stars of low complexity show a decrease of  $\Upsilon_i$  between  $0 < t \lesssim 110$  (see the two upper curves  $\Upsilon_i > 0.2$  and  $> 0.4$ ) whereas the number of stars on orbits giving a diagnostics of high-complexity remains approximately constant. This argues against border effects reaching beyond  $t \approx 20$ . The constant evolution towards more orbits of low-complexity diagnostics drive the trend of  $\Upsilon_{\text{tot}}$  observed on Fig. 15, a statement that the system suffers from collisional effects when stars are shifted to higher-energy long-period orbits by two-body collisions. Inspection of the rapid evolution of the core-radius comforts this view.

- Regime 2 begins around  $t \simeq 165$  when the system enters post-collapse and the central volume expands systematically. This triggers a sudden drop in the DWaTIM from  $\approx 0.35$  to  $\approx 0.27$  at  $t \simeq 180$ .

- Regime 3 begins (loosely speaking) at  $t \simeq 180$  units when the run of  $\Upsilon_{\text{tot}}$  resumes a slow decrease on the average. This contrast in DWaTIM orbital complexity between the pre- and the post-collapse evolution has been seen in a set of ten  $N = 256$  test simulations we performed with different random seeds. An attempt to obtain ensemble averaged results for this set of simulations proved fruitless owing to large scatter e.g., in the core-collapse time between two individual runs.

## 5 DISCUSSION

We presented a method to compute the time-dependent orbital complexity in  $N$ -body simulations. The gravitational  $N$ -body problem is described by the  $3N$  second order ordinary differential equations of Eq. (1). We extract a discrete wavelet transform information measure (DWaTIM) from the velocity time series of the individual particles of the  $N$ -body simulation. We apply the technique to several few-body problems and to a larger  $N = 256$  particle simulation. The method captures the time-dependent changes in the dynamics of three- and five-body systems and furthermore quantifies orbital complexity continuously in time. For example, we recovered and quantified the dynamically more complex phases of the well-studied Pythagorean problem (see §3.2) as well as the complex dynamics of a perturbed Caledonian configuration (see §3.3). We also applied the method to a set of  $N = 256$  equal-mass Plummer spheres (see §4). We found that, on a global scale, orbital complexity decreases during the evolution. The occurrence of core-collapse and the subsequent core expansion causes a considerable drop in overall DWaTIM complexity  $\Upsilon_{\text{tot}}$ . Furthermore, we observed that the complexity of individual orbits with a DWaTIM  $\Upsilon_i \geq 0.5$  ( $i = 1, \dots, N$ ) at the instant of core-collapse tends to increase until the occurrence of core expansion.

We opted for a DWaTIM implementation that allowed 1) to identify qualitative changes in orbital dynamics in a quasi-instantaneous manner and 2) to provide a continuous quantification of time-dependent complexity on a well-

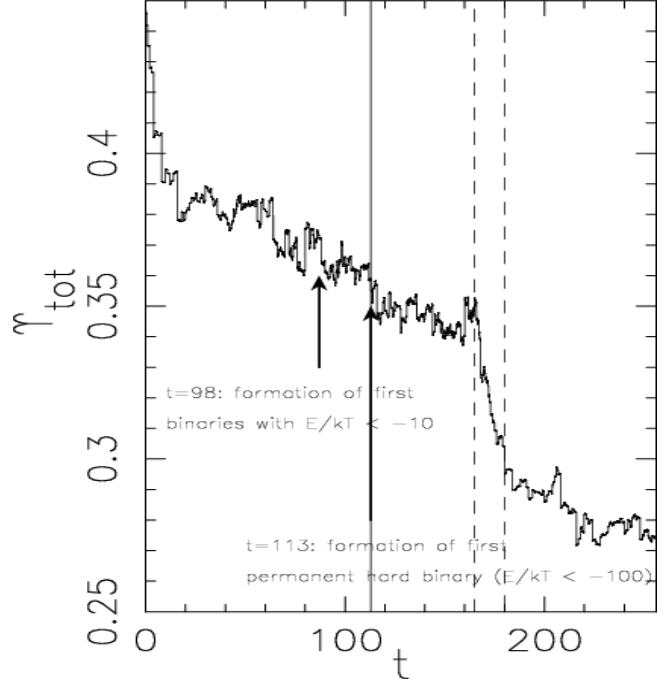


**Figure 15.** Overall DWaTIM complexity  $\Upsilon_{\text{tot}}$  for an  $N = 256$  equal-mass Plummer sphere. The curve is the average of  $\Upsilon_i$  over all  $N$  particles and over the three velocity time series in each case (the  $x$ -,  $y$ - and  $z$ - components). The solid vertical line at  $t = 113$  together with the right-most arrow mark the formation of the first hard (stable)  $E/kT < -100$  binary in the system. The left-most arrow marks the time when the first soft (unstable)  $E/kT < -10$  binary formed. The dashed vertical lines between  $165 \lesssim t \lesssim 180$  bracket the period of expansion of the inner volume.

defined gauge between 0 and 1. One should however bear in mind that an *absolute* measure of complexity of a dynamical system cannot be obtained by the method. Complexity ultimately depends on the range of scales over which the system is studied. The DWaTIM is a band-limited measure and therefore strongly depends on the resolution of the time series that is subjected to analysis. Experience drawn from several test cases shows that a repeat calculation with truncated frequency range is desirable to confirm the convergence of the diagnostics.

Border effects are an unwanted artifact of the wavelet transform. In order to reduce the bias so introduced we opted to implement a *discrete* wavelet transform and to select cubic spline functions as mother wavelets. This DWaT implementation avoids redundant wavelet coefficients. This helps in obtaining a proper measure of complexity for the two limiting cases of a unique base frequency sinusoid (DWaTIM = 0) and of a white noise signal (DWaTIM = 1), and thus to recover a well-defined gauge of complexity. We obtain reliable diagnostics of complexity whenever the orbit is integrated over a minimum of 8 complete oscillations (see §3.2).

The method is computationally inexpensive. For example, the analysis of a time series of length  $Q = 2^{13}$  data points takes approximately 1 second on a Pentium IV 2.4 GHz workstation with 1.2 GB RAM memory. It is then possible to obtain a complexity diagnostic of an  $N = 10^5$  body



system in about 80 processor-hours. A parallel implementation of the scheme is currently under development.

## ACKNOWLEDGMENTS

We would like to thank the referee, Daniel Carpintero, for a critical reading of an earlier version of this manuscript and for his helpful comments. The work was supported by grant BFR-04/55 of the Ministry for Higher Education and Research, Grand-Duchy of Luxembourg and by NWO under grant number 643.200.503. Additional support was provided by the European Doctoral College (EDC) in Strasbourg, France, by LKBF and the Netherlands Advanced School for Astrophysics (NOVA).

## REFERENCES

- Aarseth S.J., 1985, *Multiple Time Scales*, ed. U.J. Brackhill & B.I. Cohen, Orlando Academic Press, Orlando
- Aarseth S.J., Lecar M., 1975, *ARA&A*, 13, 1
- Aarseth S.J., Hénon M., Wielen R., 1974, *A&A*, 37, 183
- Aarseth S.J., Anosova J.P., Orlov V.V., Szebehely V.G., 1994, *CeMDA*, 58, 1
- Ahuja N., Lertrattanapanich S., Bose N.K., 2005, *IEE Proc.-Vis. Image Signal Process.*, 152, 659
- Benettin G., Galgani L., Strelcyn J., 1976, *Phys. Rev. A*, 14, 2338
- Binney J., Tremaine S., 1987, *Galactic Dynamics*, Princeton Series in Astrophysics
- Burrau C., 1913, *Astron. Nachr.*, 195, 113
- Carmona R., Hwang W., Torresani B., 1998, *Practical time-frequency analysis: continuous wavelet and Gabor transforms, with an implementation in S*, Wavelet Analysis and its Applications, Vol. 9, Academic Press, San Diego
- Carpintero D.D., Aguilar L.A., 1998, *MNRAS*, 298, 1
- Casertano S., Hut P., 1985, *ApJ*, 298, 80
- Cincotta P.M., Simó C., 2000, *A&A Supp.*, 147, 205
- Cohen A., Daubechies I., Feauveau J.-C., 1992, *Comm. Pure Appl. Math.*, 45, 485
- Daubechies I., 1992, *Ten Lectures on Wavelets*, Philadelphia: SIAM
- Gemmeke J.F., Portegies Zwart S.F., Kruip C.J.H., 2008, *Comm. Nonlin. Sc. Num. Sim.* 13, 1157
- Goodman J., Heggie D.C., Hut P., 1993, *ApJ*, 415, 715
- Heggie D.C., Mathieu R.D., 1986, *Lect. Notes in Phys.*, 267, 233
- Helmi A., Gómez F., 2007, *MNRAS*, submitted (arXiv:0710.0514v1)
- Hemsendorf M., Merritt D., 2002, *ApJ*, 580, 606
- Hubbard B.B., 1998, *The World According to Wavelets*, 2nd ed., A.K. Peters, Wellesley, MA
- Kandrup H.E., Eckstein B.L., Bradley B.O., 1997, *A&A*, 320, 65
- Kandrup H.E., Sideris I.V., 2001, *Phys. Rev. E*, 64, 6209
- Kandrup H.E., Sideris I.V., 2003, *ApJ*, 585, 244
- Kandrup H.E., Smith H., 1991, *ApJ*, 374, 255
- Laskar J., 1993, *CeMDA*, 56, 191
- Lo Presti L., Olmo G., 1996, *Signal Proc.*, 49, 133
- Makino J., Aarseth S.J., 1992, *PASJ* 44, 141
- Mallat S., *A Wavelet Tour of Signal Processing*, 1999, 2nd ed. San Diego, Academic Press 1999
- Martin M.T., Plastino A., Rosso O.A., 2006, *Physica A*, 369, 439
- Miller R.H., 1964, *ApJ*, 140, 250
- Miller R.H., 1971, *J. Comput. Phys.*, 8, 449
- Moortel I.D., Munday S.A., Hood A.W., 2004, *Solar Physics*, 222, 203
- Plummer H.C., 1911, *MNRAS*, 71, 460
- Portegies Zwart S., McMillan S.L.W., Hut P., Makino J., 2001, *MNRAS* 321, 1999
- Press W.H., Teukolsky S.A., Vetterling W.T., Flannery B.P., 2002, *Numerical Recipes in C++*, Cambridge University Press, Cambridge
- Quian Quiroga R., Rosso O.A., Basar E., 1999, *EEG Suppl.*, 298
- Quinlan G., Tremaine S., 1992, *MNRAS*, 259, 505
- Rosso O.A., Martin M.T., Figliola A., Keller K., Plastino A., 2006, *J. of Neurosc. Meth.*, 153, 163
- Samar V., Bopardikar A., Rao R., Swartz K., 1999, *Brain and Language*, 66, 7
- Sándor Zs., Érdi B., Efthymiopoulos C., 2000, *CeMDA*, 78, 113
- Sello S., 2003, *New Astr.*, 8, 105
- Shannon C. E., 1948, *The Bell Technical Journal*, 27, 379
- Sideris I.V., Kandrup H.E., 2002, *Phys. Rev. E*, 65, 066203
- Skokos Ch., 2001, *J. Phys. A*, 34, 10029
- Széll A., Érdi B., Sándor Zs., Steves B., 2004, *MNRAS*, 347, 380
- Thévenaz P., Blue T., Unser M., 2000, *IEEE Trans. Med. Imaging*, 19, 739
- Unser M., 1999, *IEEE Signal Process. Mag.*, 16, 22
- Valluri M., Merritt D., 1998, *ApJ*, 506, 686
- von Hoerner S., 1960, *Z. Ap.*, 50, 184